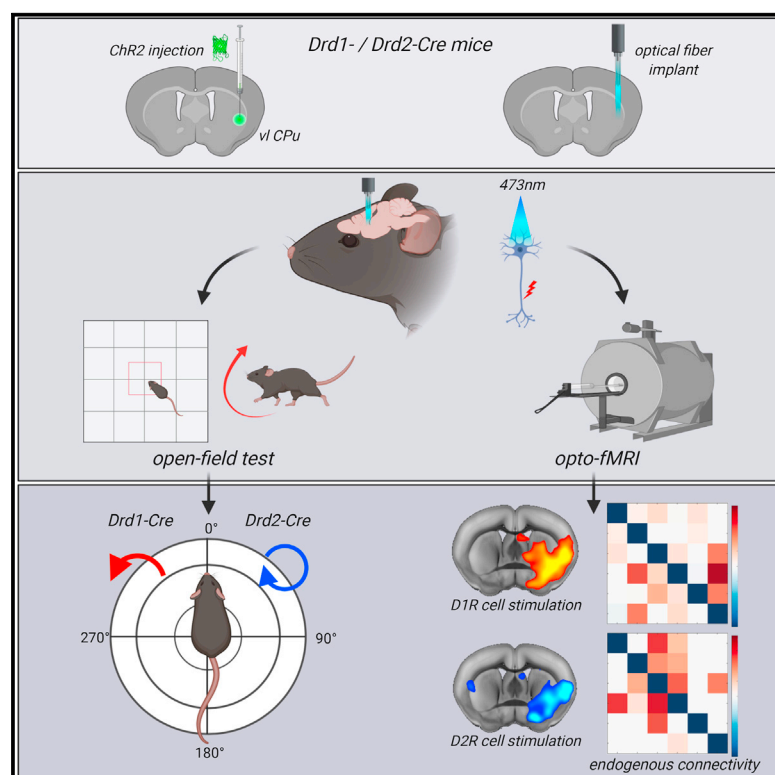


## Optogenetic activation of striatal D1R and D2R cells differentially engages downstream connected areas beyond the basal ganglia

### Graphical abstract



### Authors

Christina Grimm, Stefan Frässle, Céline Steger, ..., Daniel Razansky, Nicole Wenderoth, Valerio Zerbi

### Correspondence

valerio.zerbi@hest.ethz.ch

### In brief

Grimm et al. report that cells located in the mouse ventrolateral striatum that express D1 (D1R) and D2 (D2R) dopamine receptors differentially recruit areas within the basal ganglia-thalamocortical network and differentially modulate prefrontal and cerebellar regions.

### Highlights

- Activity modulation of striatal D1R/D2R cells via optogenetics-fMRI
- D1R/D2R cells recruit distinct areas in the basal ganglia-thalamocortical network
- Striatal D1R/D2R cells differentially modulate prefrontal and cerebellar regions
- Regression dynamic causal modeling reveals D1R/D2R output-driven relationships



Grimm et al., 2021, Cell Reports 37, 110161  
 December 28, 2021 © 2021 The Author(s).  
<https://doi.org/10.1016/j.celrep.2021.110161>

## Article

# Optogenetic activation of striatal D1R and D2R cells differentially engages downstream connected areas beyond the basal ganglia

Christina Grimm,<sup>1,9</sup> Stefan Frässle,<sup>2</sup> Céline Steger,<sup>9,10</sup> Lukas von Ziegler,<sup>3,9</sup> Oliver Sturman,<sup>3,9</sup> Noam Shemesh,<sup>4</sup> Daria Peleg-Raibstein,<sup>5,6</sup> Denis Burdakov,<sup>5,6,9</sup> Johannes Bohacek,<sup>3,9</sup> Klaas Enno Stephan,<sup>2</sup> Daniel Razansky,<sup>7,8,9</sup> Nicole Wenderoth,<sup>1,9</sup> and Valerio Zerbi<sup>1,9,11,\*</sup>

<sup>1</sup>Neural Control of Movement Lab, Department of Health Sciences and Technology, ETH Zürich, Zürich, Switzerland

<sup>2</sup>Translational Neuromodeling Unit (TNU), Institute for Biomedical Engineering, University of Zürich and ETH Zürich, Zürich, Switzerland

<sup>3</sup>Laboratory of Molecular and Behavioral Neuroscience, Institute for Neuroscience, Department of Health Sciences and Technology, ETH Zürich, Zürich, Switzerland

<sup>4</sup>Champalimaud Research, Champalimaud Centre for the Unknown, Lisbon, Portugal

<sup>5</sup>Laboratory of Neurobehavioral Dynamics, Department of Health Sciences and Technology, Institute for Neuroscience, ETH Zürich, Zürich, Switzerland

<sup>6</sup>Institute for Biomedical Engineering and Institute of Pharmacology and Toxicology, Faculty of Medicine, University of Zurich, Zürich, Switzerland

<sup>7</sup>Institute for Biomedical Engineering, Department of Information Technology and Electrical Engineering, ETH Zürich, Zürich, Switzerland

<sup>8</sup>Institute of Biological and Medical Imaging (IBMI), Technical University of Munich and Helmholtz Center Munich, Munich, Germany

<sup>9</sup>Neuroscience Center Zurich, ETH Zürich and University of Zurich, Zürich, Switzerland

<sup>10</sup>Center for MR Research, University Children's Hospital Zurich, Zürich, Switzerland

<sup>11</sup>Lead contact

\*Correspondence: [valerio.zerbi@hest.ethz.ch](mailto:valerio.zerbi@hest.ethz.ch)

<https://doi.org/10.1016/j.celrep.2021.110161>

## SUMMARY

The basal ganglia (BG) are a group of subcortical nuclei responsible for motor and executive function. Central to BG function are striatal cells expressing D1 (D1R) and D2 (D2R) dopamine receptors. D1R and D2R cells are considered functional antagonists that facilitate voluntary movements and inhibit competing motor patterns, respectively. However, whether they maintain a uniform function across the striatum and what influence they exert outside the BG is unclear. Here, we address these questions by combining optogenetic activation of D1R and D2R cells in the mouse ventrolateral caudoputamen with fMRI. Striatal D1R/D2R stimulation evokes distinct activity within the BG-thalamocortical network and differentially engages cerebellar and prefrontal regions. Computational modeling of effective connectivity confirms that changes in D1R/D2R output drive functional relationships between these regions. Our results suggest a complex functional organization of striatal D1R/D2R cells and hint toward an interconnected fronto-BG-cerebellar network modulated by striatal D1R and D2R cells.

## INTRODUCTION

The basal ganglia (BG) integrate information from a wide array of cortical and thalamic inputs and take part in the regulation of motor, cognitive, and limbic functions (Albin et al., 1989). An essential prerequisite for selection and execution of appropriate actions is the convergence of excitatory (glutamatergic) and modulatory (dopaminergic) afferents in the striatum. Striatal neurons expressing D1 and D2 receptors (D1R/D2R) constitute the major recipients of those synaptic inputs. Traditionally, their role in the striatum is associated with motor function, conveyed via the direct and indirect pathways (Albin et al., 1989; DeLong, 1990). D1R neurons of the direct pathway directly innervate the GABAergic BG-output nuclei (the substantia nigra pars reticulata [SNr] and internal globus pallidus [GPi]), which results in the

disinhibition of thalamocortical circuits, allowing them to execute commands necessary for movement initiation. Conversely, D2R neurons of the indirect pathway indirectly activate the SNr via the external globus pallidus (GPe) and the subthalamic nucleus (STN), resulting in the inhibition of thalamocortical circuits and a decrease in locomotor activity.

Although this canonical model is relevant for understanding BG-related disorders and therapeutic interventions, it assumes that D1R and D2R cells maintain their functional roles uniformly across the striatum. Contrary to this view, tracer studies in non-human primates and rodents have revealed a much more complex anatomical picture (Alexander et al., 1986; Berendse et al., 1992; Oh et al., 2014; Pan et al., 2010), with recent work counting as many as 29 anatomically distinct sub-regions in the mouse dorsomedial (dm) striatum (i.e., caudoputamen



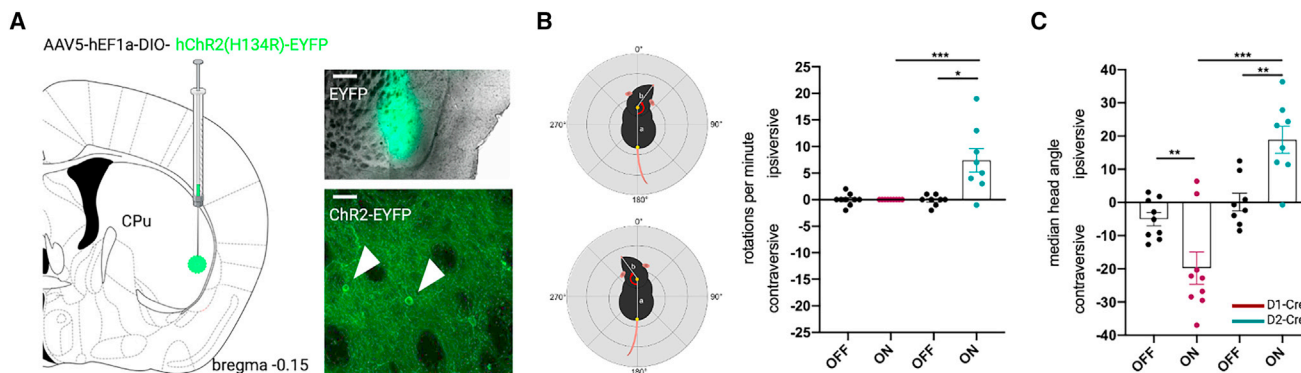


**Figure 1. Optogenetically evoked D1R and D2R cell activity in the vl CPu**

(A) Histological verification of ChR2-EYFP targeting in the vl CPu.

(B) Optogenetically evoked motor behavior measured as number of rotations per minute in the open-field test. In D1-Cre mice, rotational behavior did not increase during laser stimulation ( $n = 9$  animals;  $p = 0.876$ , two-tailed paired  $t$  test). In D2-Cre mice, the number of ipsiversive rotations per minute significantly increased during laser stimulation ( $n = 8$  animals,  $^{*}p = 0.01$ , two-tailed paired  $t$  test).

(C) Optogenetically evoked moto-behavioral effects on median head angle position in the open-field test. Optogenetic stimulation evoked highly significant changes in median head angle in D1 versus D2-Cre mice ( $^{***}p = 0.0002$ , linear mixed effects model with *post hoc* test). Specifically, laser stimulation in D2-Cre mice evoked significant changes in the head angle position in an ipsiversive manner ( $^{**}p = 0.003$ , linear mixed effects model with *post hoc* test), while D1-Cre mice changed their head angle in a contraversive manner ( $^{**}p = 0.009$ , linear mixed effects model with *post hoc* test). DYN, dynorphin; ENK, enkephalin;  $^{**}p < 0.01$ ,  $^{***}p < 0.001$ . Scale bars, 50  $\mu\text{m}$ , 500  $\mu\text{m}$ .

[CPu]] (Foster et al., 2021; Hintiryan et al., 2016). Furthermore, anatomical connections in the form of collateral branches, recurrent networks, and feedback loops suggest a causal influence of D1R and D2R cells on brain regions beyond those considered by canonical BG models, such as cerebellum and prefrontal cortex (Bostan et al., 2010; Chen et al., 2014; Hoshi et al., 2005; Ichinohe et al., 2000).

So far, however, it remains elusive how D1R and D2R cells distinctly affect the function of the circuits inside and outside the BG and whether this depends on their anatomical location in the striatum. To date, only one study has investigated large-scale functional influences of cell-type-specific activity in the mouse striatum and has provided direct evidence for the canonical model of BG motor function (Bernal-Casas et al., 2017; Lee et al., 2016). However, this analysis was restricted to the dm sub-region of the CPu.

To gain further insight into how D1R and D2R cells in other striatal sub-regions drive activity and functional interactions across the whole brain, we combined optogenetic stimulation of D1R and D2R cells in the mouse ventrolateral (vl) CPu with whole-brain functional magnetic resonance imaging (fMRI) recordings and a model of effective connectivity (regression dynamic causal modeling [rDCM]; Frässle et al., 2017, 2018, 2020). Our data show highly reproducible but different brain activation profiles during D1R and D2R cell stimulation in the vl CPu. These results confirmed that the causal role of D1R and D2R cells in BG function in line with the canonical model of the BG-thalamocortical network (Lee et al., 2016). In addition, we observed a distinct involvement of the cerebellum and prefrontal regions depending on the stimulated cell type. This information is useful for understanding the role and complexity of striatal D1R and D2R cell output and for extending the canonical description of BG function to the whole brain.

## RESULTS

### Optogenetic targeting of D1R and D2R cells in the ventrolateral striatum

For selective, light-driven activation of D1R and D2R cells, we stereotactically injected a virus carrying an excitatory opsin in the right vl CPu of D1- and D2-Cre mice (Figure 1A) (Gong et al., 2007). A 90° bent optical fiber was implanted above the targeted region to enable laser-light delivery. Histological staining confirmed that viral expression of the opsin ChR2 was located to the targeted vl CPu (Figure 1A). Next, we sought to assess the behavioral relevance of light-driven increased D1R and D2R cell activity in the open-field test. Previous reports of optogenetic D1R and D2R cell stimulation in the right dm CPu describe an increase in ipsiversive and contraversive rotations in D2- and D1-Cre mice, respectively (Kravitz et al., 2010; Lee et al., 2016), which we aimed to replicate. After an acclimatization period of 15 min, five cycles of 20-s, 20-Hz laser pulses at 5 mW (on) were delivered to the targeted cell population interleaved by 40-s periods (off) without laser stimulation. Our results show a significant difference in head angle rotations specific to D1R versus D2R cell stimulation ( $p = 0.0002$ , linear mixed effects model with *post hoc* test; Figure 1C). In D2-Cre mice, significant changes in ipsiversive median head angle position ( $p = 0.003$ , linear mixed effects model with *post hoc* test; Figure 1C) were accompanied by a significant increase in ipsiversive rotations ( $p = 0.01$ , two-tailed paired  $t$  test; Figure 1B). In D1-Cre mice, laser stimulation evoked dystonic, contraversive changes in median head angle ( $p = 0.009$ , linear mixed effects model with *post hoc* test; Figure 1C), which coincided with a significant drop in average speed ( $p = 0.03$ , linear mixed effects model with *post hoc* test; Figure S1B). These data indicate that optogenetic stimulation of D1R and D2R cells was sufficient to elicit changes at the behavioral level and show that movement patterns evoked

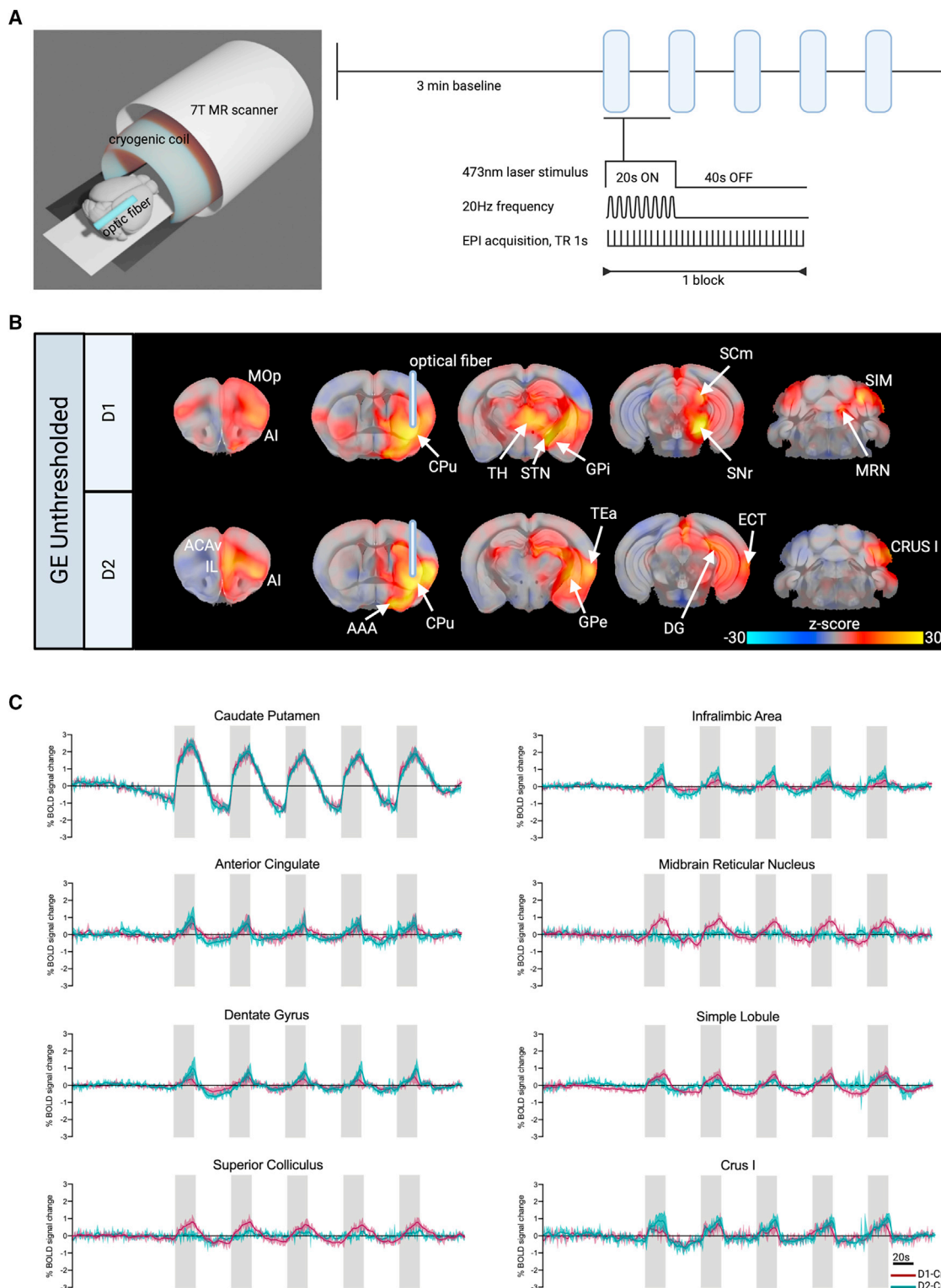


**Figure 2. Opto-fMRI reveals causal brain-wide influences of D1R and D2R cell activity**

(A) Schematic opto-fMRI setup and stimulation protocol.

(B) Unthresholded GLM z-stat activation maps of D1R and D2R cell stimulation.

(C) Mean time series of D1-/D2-Cre mice extracted from selected regions of interest based on GE-BOLD local activation maxima and minima z-stat maps. D1-Cre time series depicted in maroon, D2-Cre time series depicted in teal. Laser stimulation blocks indicated in grey. N(D1-Cre) = 11, n(D2-Cre) = 8. TR, repetition time; (legend continued on next page)



by increased activity of D1R cells in the vl CPU differ from those observed when stimulating in the dm CPU.

Following behavioral characterization, we proceeded to validate Chr2 activity on a molecular level using the neural activity marker cFos. Lightly anesthetized D1- and D2-Cre mice were stimulated for 3 min with continuous 20-Hz laser pulses at 473 nm and 3 mW. After 90 min, their brains were collected to immunohistochemically label cFos-positive D1R and D2R neurons. In both D1- and D2-Cre mice, cFos expression co-localized with the majority of Chr2-EYFP-positive cells (Figures S1D and S1E). Further, no cFos expression was found in the adjacent cortical region (Figure S1H and S1I), suggesting that our optogenetic stimulation selectively targeted the vl CPU and was sufficient to elicit changes at the molecular level.

### **Striatal D1R and D2R cell stimulation differentially engages downstream connected brain regions in and beyond the basal ganglia**

To gain insight into downstream influences of either cell population in the vl CPU, we measured whole-brain responses induced by optogenetic stimulation of D1R versus D2R cell using blood-oxygen-level-dependent (BOLD) fMRI. Correct fiber placement to the vl CPU was verified for each mouse via T1-weighted anatomical scans (Figure S2A). For the acquisition of functional scans, five cycles of 20-s blue-light laser pulse trains at 20 Hz (on) followed by a 40-s post-stimulation period (off) were applied to evoke robust brain-wide activation patterns (Figure 2A). D1-Cre mice expressing no opsin but implanted with an optical fiber in the right vl CPU were used as controls. Using a generalized linear model (GLM) approach, we identified the brain areas that were significantly modulated by the laser stimulation with voxel resolution (200  $\mu$ m isotropic; Figure 2B) and extracted their mean fMRI time series (Figures 2C and S3). Group activation maps showed brain-wide BOLD activity patterns evoked by D1R and D2R cell stimulation. We observed strong and nearly identical BOLD signal increases in the target region (Figure 2C), suggesting that we successfully matched stimulation strength in both conditions. Importantly, no BOLD changes were recorded in the vl CPU of control mice (Figure S2B). Key regions connected to the BG, like the thalamus (TH) and primary motor cortex (MOp), exhibited BOLD activation patterns in line with the canonical description of the direct pathway (Figures 2B and S3A). Contrary to the predictions of the canonical model, stimulating D1R cells evoked positive BOLD signal changes in the STN and GPi (Figure 2B). Further discrepancies with the canonical model were recorded in the GPe, where positive BOLD signal changes opposed its presumed inhibition during D2R cell stimulation (Figure S3A). Beyond the BG, D1- and D2-Cre mice showed comparable BOLD profiles in the ipsilateral agranular insula (AI), the anterior amygdalar area (AAA), and the temporal association area (TEa) (Figures S2C and S3B), while other extra-BG regions exhibited differences in their BOLD activity (Figures 2B and 2C): D2R cell activation resulted in positive BOLD responses in the

anterior cingulate (ACAv) and infralimbic (IL) area of the mPFC, the dentate gyrus (DG), and the cerebellar Crus I region. Instead, the midbrain reticular nucleus (MRN) and motor-related superior colliculus (SCm) as well as the cerebellar simple lobule (SIM) showed increased BOLD activity upon D1R cell stimulation (Figures 2B and 2C). These results provide evidence of D1R and D2R cell activity-dependent canonical and non-canonical modulation of distinct brain regions within and beyond the BG.

### **Activity of striatal, D2R-positive medium spiny neurons selectively affect BOLD profiles in regions of the indirect pathway**

Given that striatal cholinergic interneurons (ChI) express D2Rs as well, they could in part contribute to the BG BOLD profiles seen in D2-Cre mice (Alcantara et al., 2003). To account for this possibility, we additionally investigated BOLD signals upon optogenetic stimulation of the vl CPU in A2A-Cre mice, which exclusively express Cre in D2 medium spiny neurons (MSNs). Importantly, Chr2 expression as well as the direction of BOLD responses in the targeted vl CPU of A2A-Cre mice was identical to that of D2-Cre mice, suggesting matched stimulation effects of D2R cells in vl CPU in both mouse lines (Figures 2B, 2C, S4A, and S4B). We further observed comparable BOLD activation patterns in the ipsilateral GPi, SNr, and STN (Figure S4C). Notably, as seen in D2-Cre datasets, no changes in BOLD activity were recorded in the ipsilateral TH (Figures 2B and S4C). These similarities constituted a strong positive correlation of BOLD signal changes in the BG-thalamocortical pathway between A2A- and D2-Cre mice (Pearson's  $r(5) = 0.89$ ,  $p = 0.007$ ; Figure S4D). Contrary to D2-Cre datasets but in line with the canonical model of BG function, BOLD signals in the MOp decreased while no significant BOLD activity was recorded in the GPe (Figure S4C). When comparing D1 and A2A-Cre datasets, no significant correlations were found in areas within the BG-thalamocortical network (Pearson's  $r(5) = 0.38$ ,  $p = 0.053$ ; Figure S4E). Taken together, these findings suggest that a potential co-activation of D2R MSNs in D2-Cre mice could contribute to BOLD activity profiles in select regions of the indirect pathway.

### **Striatal D1R and D2R cell stimulation differentially alters dynamics of functional brain responses**

After having characterized the spatial extent of D1R and D2R cell activation, we focused on further elucidating the dynamics of these functional brain responses. One way to do this is to use dimensionality reduction techniques (Tononi et al., 1999). These approaches can uncover latent functional patterns in complex datasets by distilling high-dimensional brain activity patterns into a small number of low-dimensional spatiotemporal components (Cunningham and Yu, 2014). After concatenating the datasets, each repetition time block (1 s) was projected onto a low-dimensional space using an unsupervised manifold learning technique (Uniform Manifold Approximation

EPI, echo planar imaging; AAA, anterior amygdalar area; AI, agranular insula; ACAv, anterior cingulate; CPU, caudate putamen; TH, thalamus; SNr, substantia nigra; SSp-bfd, primary somatosensory cortex, barrel field; SCm, superior colliculus, motor related; STN, subthalamic nucleus; TEa, temporal association area; ECT, ectothalamic area; IL, infralimbic area; GPe, external globus pallidus; DG, dentate gyrus; MOp, primary motor cortex; MRN, midbrain reticular nucleus; SIM, simple lobule.

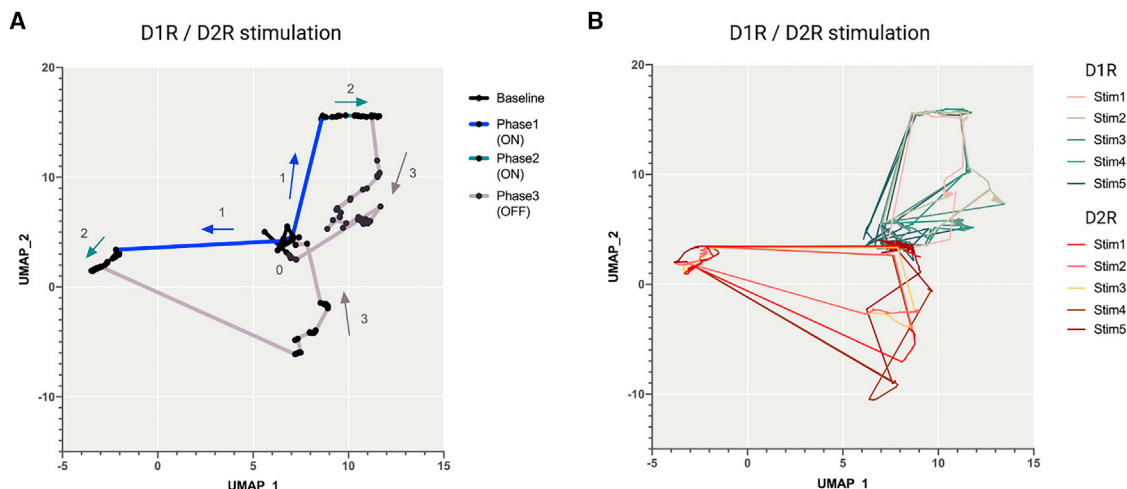


**Figure 3. Functional brain-wide responses dynamically change upon D1R and D2R cell stimulation**

(A) Low-dimensional representation of averaged stimulation blocks in D1- and D2-Cre fMRI datasets.

(B) Low-dimensional representation of single stimulation blocks in D1- and D2-Cre fMRI datasets. UMAP, Uniform Manifold Approximation and Projection. N(D1-Cre) = 11, n(D2-Cre) = 8.

and Projection [UMAP]) (Becht et al., 2018). The point-to-point trajectories in the UMAP plots were then used to interpret the dynamics of the D1R and D2R stimulations and to evaluate the reproducibility of the activation patterns across the five stimulation blocks. Both datasets showed a response to the optogenetic stimulation in three phases (Figures 3A and 3B). However, the observed patterns formed distinct trajectories in the low-dimensional manifold, indicating that their activation engages different brain areas (Figures 3C, 3D; Videos S1, and S2). Both stimulations evoked an initial rapid response to the delivered laser stimulus lasting 1 to 2 s (phase 1) followed by a sustained response for the remainder of the stimulation (18–19 s, phase 2; Figures 3A and 3B). Once laser stimulation was terminated, BOLD activity in D1- and D2-Cre datasets gradually returned to baseline levels (39–40 s, phase 3; Figures 3A and 3B). This indicates that, despite the engagement of different brain regions, BOLD activation patterns during D1R and D2R cell stimulation followed similar and highly reproducible dynamics.

### Different fMRI contrasts capture robust brain-wide activation patterns of D1R and D2R cell stimulation

In addition to the classical gradient-echo (GE)-BOLD, select fMRI sequences allow adjustment of the sensitivity of scans to their contrast types, which in turn influences functional activation patterns. Here, we rescanned experimental mice using two additional fMRI sequences with different intrinsic contrasts; namely, a spin-echo (SE) that enhances BOLD contrast from microcapillaries (Keilholz et al., 2006; Lee et al., 1999; Zhao et al., 2004), and a diffusion-weighted functional scan (diffusion fMRI [dfMRI]) that is sensitive to changes in the intra- and extravascular diffusion of water molecules upon neural activation (Nunes et al., 2019, 2021). SE and dfMRI sequences alike captured D1R and D2R cell activity-dependent fMRI signal changes in key regions within the BG (Figure S5).

We next aimed to obtain a more precise anatomical delineation of the difference between D1/D2 activation profiles. To do that, we compared D1- and D2-Cre datasets in a consensus analysis across all three different functional contrasts. First, GE, SE, and dfMRI datasets were re-sampled (200  $\mu$ m isotropic) and transformed to a common template space using both linear and non-linear transformation. In a second step, contrast estimates based on GE, SE, and dfMRI acquisitions were pooled at the group level to compute a between-group statistical map, harboring group-specific activation across all three functional contrasts (Figure 4A). By comparing the brain-wide influences of each cell population, we observed that D1R cells drive stronger activity in the MOp, the MRN, the ipsi- and contralateral SIM, as well as in the ipsi- and contralateral primary somatosensory cortex, mouth area (SSp-m), while D2R cells more potently activated the ipsilateral Crus I of the cerebellum, the majority of the ipsilateral DG, the ACAv, and the IL area of the mPFC (Figure 4B). Additionally, D2R cell stimulation elicited greater engagement of the ipsilateral SSp, including the upper and lower limb, trunk, and barrel field area compared with D1R cell activity. These findings further corroborate the different roles of D1R and D2R cells in driving brain-wide dynamics in and outside the BG.

### Regression dynamic causal modeling reveals distinct network connectivity participation upon D1R and D2R cell stimulation

Traditionally, neuronal circuit models are based on the fragmented analysis of anatomical connections and individually acquired electrophysiological parameters. Current techniques, however, strive to achieve a more integrative perspective on functionally connected neural networks by uniting whole-brain functional recordings, neurostimulation, and computational modeling (Bernal-Casas et al., 2017). To infer upon the directed interactions among brain regions (i.e., effective connectivity)

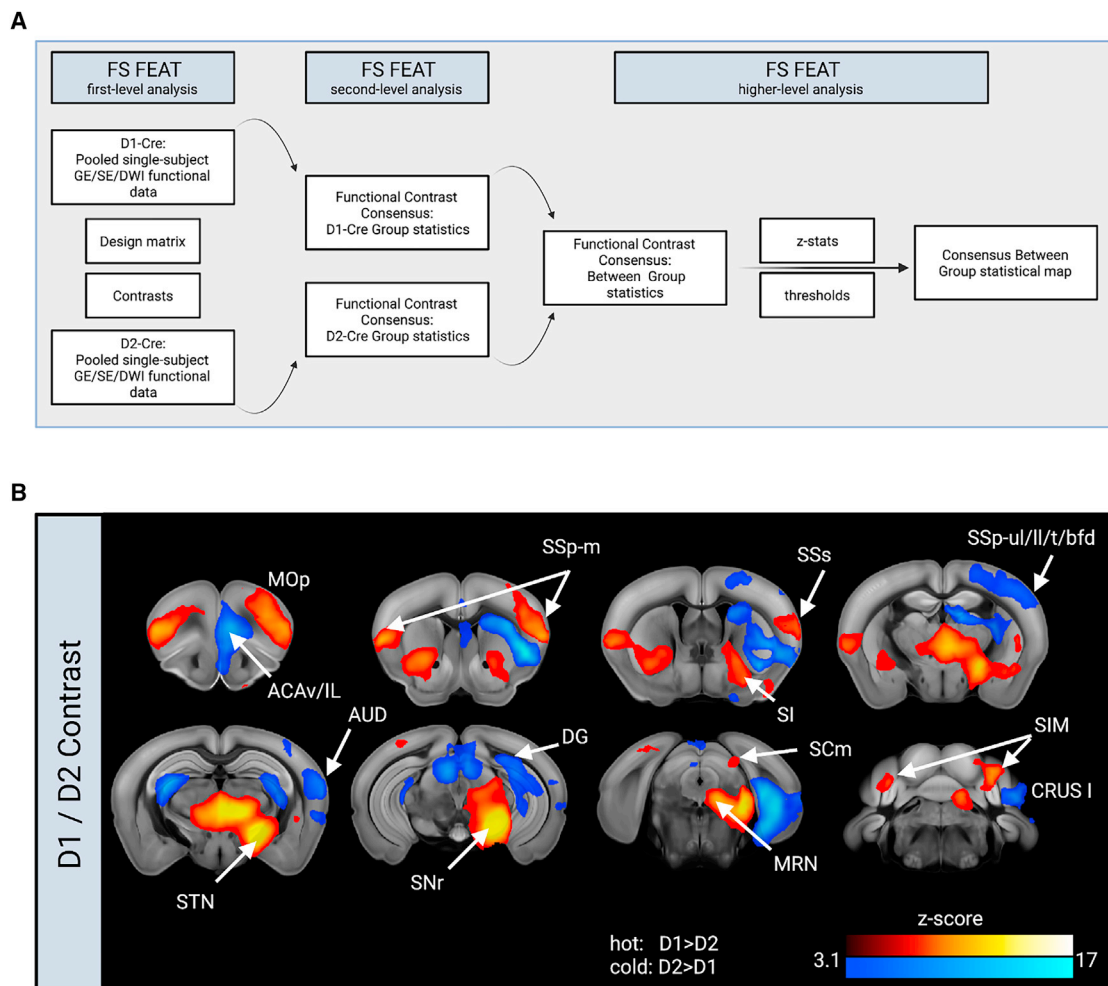


**Figure 4. D1R and D2R cells differentially activate brain regions beyond the BG**

(A) D1- and D2-Cre functional data analysis to create a GE/SE/dfMRI consensus between-group z-stat activation map using FSL FEAT.

(B) GE/SE/dfMRI consensus z-stat activation map (cluster corrected;  $p < 0.05$ ).  $N(\text{D1-Cre}) = 11$ ,  $n(\text{D2-Cre}) = 8$ . ACAv, anterior cingulate; IL, infralimbic area; AI, agranular insula; MOp, primary motor cortex; SSp-m, primary somatosensory cortex, mouth area; SSs, supplemental somatosensory area; SI, substantia innominata; SSp-bfd, primary somatosensory cortex, barrel field area; GPi, internal globus pallidus; MD, mediodorsal nucleus of thalamus; AUDp, primary auditory area; STN, subthalamic nucleus; SNr, substantia nigra; DG, dentate gyrus; SCm, superior colliculus, motor related; MRN, midbrain reticular nucleus; SIM, simple lobule. Color code cold (blue to turquoise): D2R > D1R cells.

within and beyond the BG-thalamocortical network, we applied rDCM to our opto-fMRI data.

First, we assessed effective connectivity among six key components of the canonical BG-thalamocortical network (MOp, CPu, GPe, GPi, MD, and SNr; Figure S6). Reassuringly, for both D1R and D2R cell stimulation, rDCM correctly identified the vl CPu as the input region. More specifically, using fixed-effects Bayesian model selection (BMS) to compare all possible hypotheses of which region received the optogenetic stimulation yielded decisive evidence for the correct model with vl CPu as input region (posterior model probability of 1 for both D1R and D2R cells).

Inspecting the group-level posterior parameter estimates of the winning model, we found the effective connectivity patterns to be consistent with previous studies on the functional integration in the BG-thalamocortical network (Bernal-Casas et al.,

2017). In brief, during D1R cell stimulation (Figure 5A), we observed strong efferent connections from vl CPu to GPi and SNr, but not to GPe. Furthermore, strong connections were observed from SNr to GPe and GPi. Finally, the BG-output nucleus SNr sent strong projections to MD, which in turn sent information to the motor-output region MOp. Conversely, during D2R cell stimulation, functional integration was overall weaker than during D1R cell stimulation and displayed a distinct pattern (Figure 5B). When directly comparing D1 and D2, we found connections from vl CPu to GPi and from vl CPu to SNr—the defining projections of the direct pathway—to be significantly greater during D1R compared with D2R cell stimulation (Figure 5C). Conversely, the connection from vl CPu to GPe, a key region of the indirect pathway, was significantly increased during D2R compared with D1R cell stimulation. Furthermore, functional integration between GPi and SNr, as well as from the BG-output

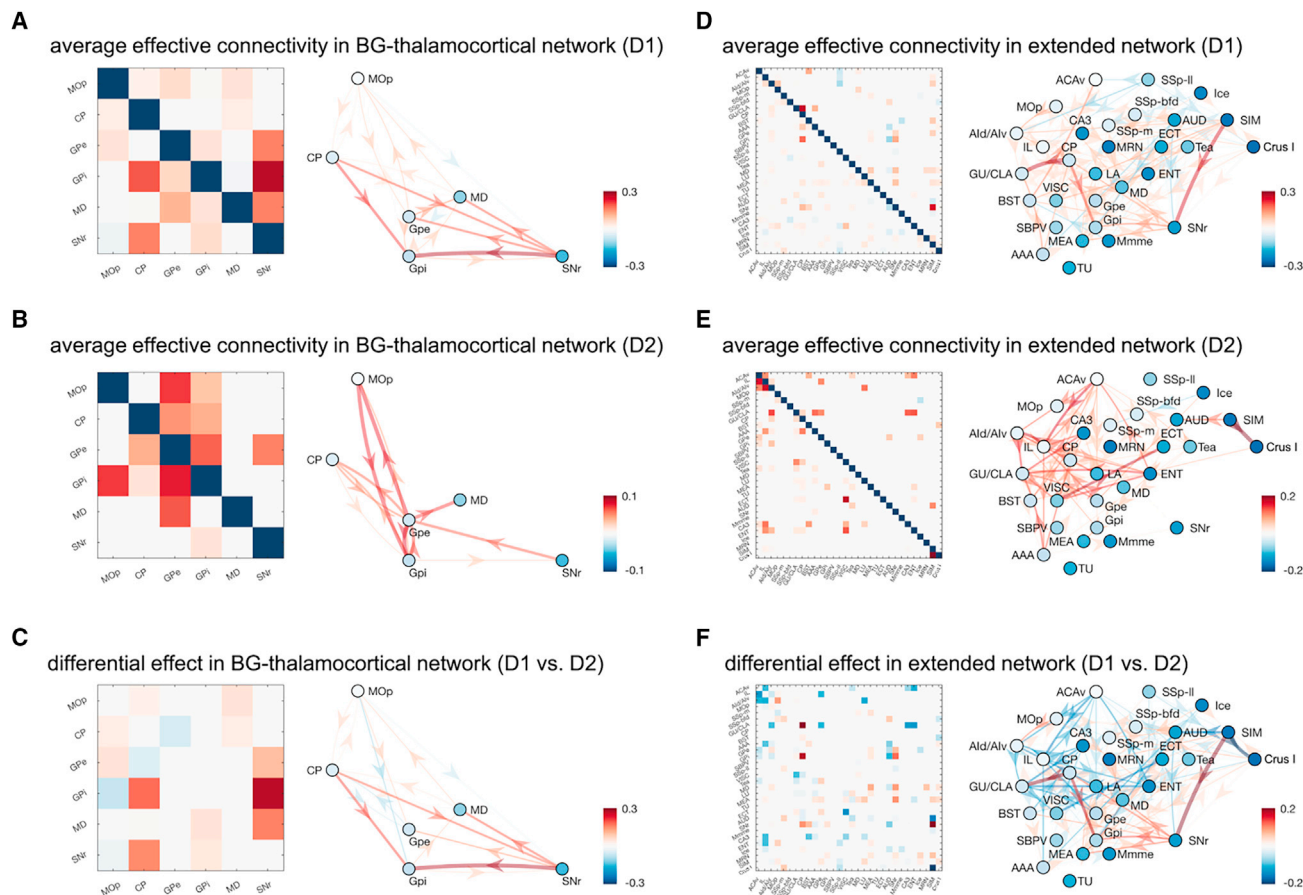


**Figure 5. Effective (directed) connectivity during D1R or D2R cell stimulation as inferred using rDCM**

(A and B) Average connectivity pattern in the BG-thalamocortical network during D1R cell stimulation (A) and during D2R cell stimulation (B) ( $p > 0.95$ ).

(C) Differential effect of the optogenetic stimulation (D1-D2) in the BG-thalamocortical network ( $p > 0.95$ ), where red colors indicate stronger connections during D1 stimulation and blue colors indicate stronger connections during D2 stimulation.

(D and E) Average connectivity pattern in the extended network during D1R cell stimulation (D) and during D2R cell stimulation (E) ( $p > 0.95$ ).

(F) Differential effect of the optogenetic stimulation (D1-D2) in the extended network ( $p > 0.95$ ), where red colors indicate stronger connections during D1R cell stimulation and blue colors indicate stronger connections during D2R cell stimulation. Note, color maps of each subplot have been adjusted to the respective maximal absolute connection strength and may thus differ between subplots.  $N(D1-Cre) = 11$ ,  $n(D2-Cre) = 8$ . AAA, anterior amygdalar area; ACAV, anterior cingulate; PrL, prelimbic area; Alv, ventral agranular insula; AUD, auditory area; BST, Bed nuclei of the stria terminalis; CA3, Ammon's horn field 3; CPu, caudate putamen; ECT, entorhinal area; ENT, entorhinal area; GPe, external globus pallidus; GPi, internal globus pallidus; GU/CLA, gustatory area/claustrum; Ice, inferior colliculus; IL, infralimbic area; LA, lateral amygdala nucleus; MEA, medial amygdala nucleus; MD, mediodorsal nucleus of thalamus; Mmme, medial part of the medial mammillary nucleus; MOp, primary motor cortex; MRN, midbrain reticular nucleus; SIM, simple lobule; SNr, substantia nigra pars reticulata; SBPV, subparaventricular zone; SSp-bfd, primary somatosensory cortex, barrel field; SSp-II, primary somatosensory cortex, lower limb area; SSp-m, primary somatosensory cortex, mouth area; TEa, temporal association area; TU, tuberal nucleus; VISC, visceral area.

nucleus SNr to GPe and MD was greater during D1R compared with D2R cell stimulation. In addition to the aforementioned differences, other connections showed a significant differential effect of the optogenetic stimulation (Figure 5C).

In a next step, we investigated functional integration beyond the BG in an extended brain-wide network, including all regions in the mouse brain that were jointly activated or deactivated by D1R and D2R cell stimulation. Again, we first verified that rDCM correctly identified vl CPu as the target region that received the optogenetic stimulation for both D1R and D2R cells.

Inspecting the group-level posterior parameter estimates of the winning model, we initially verified that, in this extended

(whole-brain) analysis, the effective connectivity patterns in the BG-thalamocortical network were consistent with those obtained from the previous, more local analysis of connectivity. In brief, during D1R cell stimulation (Figure 5D), we again observed strong engagement of the defining projections of the direct pathway, namely, the efferent connections from vl CPu to GPi and SNr (Figure S7A), as well as strong connections from the BG-output nucleus SNr to MD (Figure S7B). Going beyond the canonical BG-thalamocortical network, we observed strong projections from cerebellar regions, in particular SIM, to various components of the BG-thalamocortical network, in particular, SNr but also GPe and MD (Figure S7C). Finally, we found strong efferent connections from vl CPu to gustatory area/claustrum



(GU/CLA) (Figure S7A). During D2R cell stimulation (Figure 5E), the effective connectivity patterns again differed substantially from the D1R cell stimulation. Specifically, as expected, we found no engagement of the direct pathway (Figure S7D). Instead, we observed a strong involvement of prefrontal regions (e.g., AI dorsal [Aid]/AI ventral [Alv], IL) as well as cingulate regions (e.g., ACAv) (Figure S7E). Furthermore, we observed involvement of cerebellar structures (where the strongest projection was between two cerebellar regions, from SIM to Crus I) (Figure S7F). Explicitly testing for difference between D1 and D2 revealed a wide range of differences both within the canonical BG-thalamocortical network and beyond, in prefrontal and cerebellar areas (Figure 5F).

In summary, rDCM provides further evidence that D1R and D2R cells drive activity in areas beyond the BG, involving cerebellar and prefrontal structures in a differential manner.

## DISCUSSION

Traditionally, motor function of the BG is described as a feedforward model, wherein D1R cells of the direct pathway disinhibit thalamo-cortical circuits necessary for movement initiation and D2R cells of the indirect pathway act opposingly via an increase of the BG's inhibitory control over the thalamus (Albin et al., 1989). In line with this view, we found that activation of D1R but not D2R cells in the vl CPU elicited positive BOLD responses in key structures of the direct pathway, including the TH and motor cortex. These results were further corroborated by effective connectivity analysis using rDCM, which highlighted the importance of the direct pathway during D1R but not D2R cell stimulation. Using different fMRI contrast acquisitions, we were able to attenuate signal biases from putatively vascular sources and thereby provide a solid consensus on the organization of brain-wide activation patterns driven by either cell population. Importantly, we observed different but not necessarily opposing effects of D1R and D2R cell stimulation within the BG. Beyond the BG, D1R and D2R cell stimulation differentially involved medial prefrontal regions as well as ipsi- and contralateral cerebellar lobules, which rDCM analysis also faithfully recapitulated. Our findings suggest a more complex functional organization of D1R and D2R cells across the striatum than previously anticipated and provide evidence for the existence of an interconnected fronto-BG-cerebellar network modulated by striatal D1R and D2R cells.

The behavioral output of striatal D1R and D2R cells is closely linked to motor initiation and suppression, respectively (Freeze et al., 2013). In fact, disruptions of this striatal balance have been implicated in several movement as well as neurodevelopmental disorders (Grissom et al., 2018; Kumar et al., 2018; Portmann et al., 2014). Rodent behavioral studies that stimulated D1R and D2R cells in the dm CPU have repeatedly supported their opposing roles (Freeze et al., 2013; Kravitz et al., 2010; Kreitzer and Malenka, 2007; Lee et al., 2016). When tested in the open-field test, unilateral stimulation of D2R cells in the vl CPU resulted in an increase of ipsiversive full-body rotations; a behavior that is identical to the one elicited during dm CPU D2R cell stimulation (Kravitz et al., 2010; Lee et al., 2016). Instead, D1R cell stimulation produced contraversive, dysto-

nia-like head and neck movements. This differs from the full-body contraversive, rotational phenotype reported in D1-Cre mice when stimulated in the dm CPU (Kravitz et al., 2010; Lee et al., 2016). In the dorsal CPU, electrophysiological studies have shown that D1R cells are less excitable than D2R cells and that concurrent activation of both cell types is necessary for contraversive movements (Cui et al., 2013; Kreitzer and Malenka, 2007). However, whether this difference between D1R and D2R cells is present in other sub-regions, like the vl CPU, and how this would affect motor behavior is yet to be investigated. Overall, our data suggest a role of D1R cells on motor behavior that is heterogeneous and dependent on their anatomical location in the CPU, while, for D2R cells, the exact location in the CPU does not seem to affect motor output.

On a more speculative note, the repetitive nature of head and neck movements in D1-Cre mice strongly resembled the clinical presentation of cervical dystonia, a syndrome of sustained or intermittent muscle contractions causing sideways twisting of the head (Hallett, 2011). Although relatively little is known about BG neuronal activity in dystonia, a recent study reported increased activity of the direct pathway in patients suffering from dystonic, involuntary movements: Simonyan et al. (Berman et al., 2013; Simonyan et al., 2013, 2017) found increased D1R availability in the striatum of dystonic patients, which was paralleled by abnormally decreased D2R function via the indirect BG pathway. Ultimately, this imbalance between D1Rs and D2Rs within the BG pathways could give rise to dystonic movement patterns (Hallett, 2011). Our findings are in line with these human findings and suggest that optogenetic stimulation of D1R cells in the vl CPU could induce such an imbalance in the BG and evoke dystonia-like movements also in mice. This assumption warrants a more thorough behavioral characterization of striatal D1R cell hyperactivity and its potential role in dystonia.

The canonical model of BG function proposes opposing effects of striatal D1R and D2R cells on BG-thalamocortical activity (Albin et al., 1989; DeLong, 1990). Using opto-fMRI, we measured the cell-type- and region-specific influences of D1R and D2R cells and tested the validity of this model within the BG circuit. We further mapped the effective (directed) connectivity among key BG regions using rDCM (Frässle et al., 2017, 2018) to infer how either cell population contributes to reshaping the functional architecture of the BG-thalamocortical network. Importantly, effective connectivity among key regions of the direct pathway was significantly increased during D1R cell stimulation, while defining projections of the indirect pathway were significantly greater during D2R cell stimulation, suggesting that their net output remains closely linked to "go"/"no-go" motor commands, respectively. Nevertheless, we found that BOLD dynamics could not support strictly antagonistic influences of vl CPU D1R and D2R cells within the BG-thalamocortical network. This included the TH and motor cortex. Here, D1R cell stimulation elicited significant BOLD signal increases, but no changes were recorded during D2R cell stimulation, which contradicted their presumed inhibition (i.e., de-activation during D2R cell activity) (Albin et al., 1989; DeLong, 1990). Further, we found no opposing effects of D1R and D2R cells on BOLD activity in the GPI and SNr. In fact, given that activation of striatal D1R and D2R cells should exert inhibitory and excitatory control over



these nuclei, respectively, their observed increased BOLD signal changes were unexpected. BOLD signals of the STN did not fit their predicted opposing profiles during D1R and D2R cell stimulation either. These findings stand in contrast to previous opto-fMRI data by [Lee et al. \(2016\)](#). Targeting the dm CPu, they showed positive BG BOLD responses during D1R cell stimulation, while negative BG BOLD responses were evoked during D2R cell stimulation. Notably, while these responses did not strictly follow predictions of the canonical model either (see [Lee et al., 2016](#) for an extensive discussion thereof), they reflected the proposed antagonistic effects of striatal D1R and D2R cells. Instead, our results indicate that, during prolonged stimulation in the vl CPu, D1R and D2R cells do not exert opposing control. Rather, they differentially engage activity, potentially via inhibitory interneurons with local synapses or projection neurons with lateral connections throughout the BG nuclei ([Oorschot, 2010](#)). This highlights the importance of considering the complex structural and functional architecture of the striatum when addressing the causal role of striatal D1R and D2R cells within the BG.

The BG are traditionally modeled as integrative structures that send and receive projections to each other and across a vast network of brain areas. Hence, we expected functional influences of striatal D1R and D2R cells to extend beyond the BG. In line with this view, we showed that D1R or D2R cell activation led to changes in BOLD activity in the mPFC and cerebellar cortices. For example, D2R cell excitation was followed by strong increases in BOLD signal in the ACAv and IL area of the mPFC, suggesting a causal influence of striatal D2R cells at this level. D2R cell activity might participate in modulating the mPFC's executive control of actions, especially those related to action inhibition ([Posner et al., 2007](#); [Ridderinkhof et al., 2004](#)). The mPFC has implications in a wide range of psychiatric diseases where executive control of action is compromised, including obsessive-compulsive disorder, addiction, and anxiety ([Snyder et al., 2015a, 2015b](#); [Snyder et al., 2015b](#)). Importantly, separate lines of evidence indicate that the rodent mPFC-CPu circuit is relevant to anxiety and avoidance behavior: using optogenetics and electrophysiology, [Friedman et al. \(2015\)](#) demonstrated that ACAv to dm CPu projections are selectively active during an approach-avoidance T-maze task and that their excitation increases avoidance behavior. Increased activity of mPFC-dm CPu projection neurons has also been reported during open arm exploration of an anxiogenic elevated zero maze (EZM) ([Loewke et al., 2021](#)). In fact, stimulation of striatal D2R cells increased avoidance in the EZM and further heightened avoidance of open areas during an open-field test ([Leblanc et al., 2020](#); [Loewke et al., 2021](#)), suggesting that striatal D2R cells are critically involved in the control of avoidance behaviors ([Friedman et al., 2015](#); [Loewke et al., 2021](#)). Our results support a causal role of D2R cells in mPFC modulation and indicate that their functional influence is not limited to motor output but also involves higher cognitive processes and executive control.

We also found differential effects of D1R and D2R cell stimulation in the cerebellum. Striatal D1R cells evoked BOLD activity in the bilateral SIM while D2R cells engaged the Crus I area. Along those lines, rDCM revealed that areas of the BG-thalamocortical

network, in particular, SNr, GPe, and MD, receive afferent inputs by SIM during D1R cell stimulation. In contrast, intra-cerebellar projections from SIM to Crus I dominated during D2R cell stimulation. Importantly, the cerebellum not only receives input and sends output to the prefrontal cortex ([Kelly and Strick, 2003](#); [Middleton and Strick, 2001](#)) but has also been shown to communicate with the BG via cerebellar motor and non-motor-output nuclei. These nuclei project di-synaptically via the intralaminar thalamic nuclei to the striatum ([Chen et al., 2014](#); [Hoshi et al., 2005](#)) and ultimately give rise to an interconnected fronto-BG-cerebellar network. This network shows topographic organization: cognitive, limbic, and motor territories of each participating brain region are functionally connected, explaining how abnormal activity in one region can affect activity at the network level ([Bostan et al., 2013](#); [Peters et al., 2019](#)). Our findings show that striatal D1R cells can reshape the functional connections within such a fronto-BG-cerebellar network and suggest a framework where D1R and D2R sub-populations differentially influence the network dynamics.

### Limitations of the study

We want to acknowledge that co-labeling of D2R-positive, striatal ChIs in the D2-Cre line is an important confound to consider when studying the function of the BG indirect pathway in this mouse line ([Alcantara et al., 2003](#)). Acetylcholine (ACh) release triggered by optogenetic stimulation of striatal D2R cells could increase activity of direct pathway D1R cells via their muscarinic acetylcholine receptors 4 (Chrm4) and therefore partly drive BOLD signals in D2-Cre mice ([Ince et al., 1997](#)). To account for this potential spill-over effect, we additionally investigated BG BOLD signal changes in A2A-Cre mice, which exclusively express Cre in indirect pathway MSNs ([Alcantara et al., 2003](#)). While the majority of indirect pathway regions followed activation profiles as seen in D2-Cre datasets, the GPe and MOp did not. With no significant change detectable in the GPe and a decrease in BOLD signal in the MOp, these regions more closely followed predictions based on the canonical model of BG function instead. The current study falls short of a more thorough investigation of these findings, which suggest that the observed signal increase in the GPe and the lack of MOp signal change in D2-Cre datasets could indeed be driven by co-activation of D2R-positive ChIs in the vl CPu. Particularly in light of potential influences of other striatal cell types that express D2Rs, including glutamatergic and DA afferents ([Bamford, 2004](#); [Gerfen et al., 1990](#)), such an assumption demands more in-depth testing than is provided here.

### Conclusions

Our study provides evidence that the functional influence of striatal D1R cells on brain activity dynamics extends beyond the BG-thalamocortical network and is of differential rather than strictly antagonistic nature. Importantly, these effects seem to be dependent on their anatomical location in the striatum. In light of these findings, we propose that revised network models of BG function should take into consideration (1) cell-type-specific influences (e.g., D1R versus D2R cells), (2) the functional architecture of key brain areas within the BG (e.g., dm CPu versus vl CPu), and (3) the involvement of regions

beyond the BG-thalamocortical network (e.g., mPFC and cerebellum). Acknowledging these factors will pave the way for a more complete understanding of BG function within large-scale networks and have important implications for a wide range of movement and psychiatric disorders.

## STAR★METHODS

Detailed methods are provided in the online version of this paper and include the following:

- **KEY RESOURCES TABLE**
- **RESOURCE AVAILABILITY**
  - Lead contact
  - Materials availability
  - Data and code availability
- **EXPERIMENTAL MODELS AND SUBJECT DETAILS**
  - Animals
- **METHOD DETAILS**
  - Stereotaxic surgery
  - Open-field test in freely moving mice
  - Opto-fMRI recording
  - Tissue collection for immunohistochemistry
  - Immunohistochemistry
- **QUANTIFICATION AND STATISTICAL ANALYSIS**
  - Open-field test in freely moving mice
  - GLM statistical mapping
  - Dimensionality reduction
  - rDCM analysis

## SUPPLEMENTAL INFORMATION

Supplemental information can be found online at <https://doi.org/10.1016/j.celrep.2021.110161>.

## ACKNOWLEDGMENTS

We thank Jean-Charles Paterna from the Viral Vector Facility (VVF) of the Neuroscience Center Zürich, a joint competence center of ETH Zürich and the University of Zürich, for producing viral vectors and viral vector plasmids. We also thank Jin H. Lee (Stanford University, United States) for the initial discussion on this project. C.G. and V.Z. are supported by the research grant ETH 062-18 and the Swiss National Science Foundation (SNSF) AMBIZIONE PZ00P3\_173984/1. J.B. is supported by the ETH Zürich, ETH project grant ETH-20 19-1, SNSF grant 310030\_172889, and the 3R Competence Center. K.E.S. acknowledges support by the SNSF (project grant 320030\_179377) and the René and Susanne Braginsky Foundation. Graphical abstract was created with BioRender.com.

## AUTHOR CONTRIBUTIONS

Conceptualization, C.G., S.F., N.W., and V.Z.; methodology, C.G., S.F., C.S., L.v.Z., O.S., N.S., and V.Z.; investigation, C.G., S.F., C.S., L.v.Z., and O.S.; writing – original draft, C.G., S.F., and V.Z.; writing – review & editing, C.G., S.F., C.S., L.v.Z., O.S., N.S., J.B., K.E.S., D.R., N.W., V.Z., D.P.R., and D.B.; funding acquisition, V.Z., J.B., K.E.S., and D.R.; supervision, J.B., K.E.S., D.R., N.W., and V.Z.

## DECLARATION OF INTERESTS

The authors declare no competing interests.

Received: March 8, 2021  
Revised: October 20, 2021  
Accepted: December 1, 2021  
Published: December 28, 2021

## REFERENCES

- Albin, R.L., Young, A.B., and Penney, J.B. (1989). The functional anatomy of basal ganglia disorders. *Trends Neurosci.* 12, 366–375. [https://doi.org/10.1016/0166-2236\(89\)90074-x](https://doi.org/10.1016/0166-2236(89)90074-x).
- Alcantara, A., Chen, V., Herring, B., Mendenhall, J., and Berlanga, M. (2003). Localization of dopamine D2 receptors on cholinergic interneurons of the dorsal striatum and nucleus accumbens of the rat. *Brain Res.* 986, 22–29. [https://doi.org/10.1016/s0006-8993\(03\)03165-2](https://doi.org/10.1016/s0006-8993(03)03165-2).
- Alexander, G.E., DeLong, M.R., and Strick, P.L. (1986). Parallel organization of functionally segregated circuits linking basal ganglia and cortex. *Annu. Rev. Neurosci.* 9, 357–381. <https://doi.org/10.1146/annurev.ne.09.030186.002041>.
- Aymanns, F., Rudin, M., and Ioannas, H.-I. (2020). COSplay: contrast optimized stimulation player. *J. Open Source Softw.* 4, 1171. <https://doi.org/10.21105/joss.01171>.
- Bamford, N.S. (2004). Dopamine modulates release from corticostriatal terminals. *J. Neurosci.* 24, 9541–9552. <https://doi.org/10.1523/jneurosci.2891-04.2004>.
- Becht, E., McInnes, L., Healy, J., Dutertre, C.A., Kwok, I.W.H., Ng, L.G., Ginhoux, F., and Newell, E.W. (2018). Dimensionality reduction for visualizing single-cell data using UMAP. *Nat. Biotechnol.* <https://doi.org/10.1038/nbt.4314>.
- Berendse, H.W., Galis-de Graaf, Y., and Groenewegen, H.J. (1992). Topographical organization and relationship with ventral striatal compartments of prefrontal corticostriatal projections in the rat. *J. Comp. Neurol.* 316, 314–347. <https://doi.org/10.1002/cne.903160305>.
- Berman, B.D., Hallett, M., Herscovitch, P., and Simonyan, K. (2013). Striatal dopaminergic dysfunction at rest and during task performance in writer's cramp. *Brain* 136, 3645–3658. <https://doi.org/10.1093/brain/awt282>.
- Bernal-Casas, D., Lee, H.J., Weitz, A.J., and Lee, J.H. (2017). Studying brain circuit function with dynamic causal modeling for optogenetic fMRI. *Neuron* 93, 522–532.e525. <https://doi.org/10.1016/j.neuron.2016.12.035>.
- Bostan, A.C., Dum, R.P., and Strick, P.L. (2010). The basal ganglia communicate with the cerebellum. *Proc. Natl. Acad. Sci.* 107, 8452–8456. <https://doi.org/10.1073/pnas.1000496107>.
- Bostan, A.C., Dum, R.P., and Strick, P.L. (2013). Cerebellar networks with the cerebral cortex and basal ganglia. *Trends Cogn. Sci.* 17, 241–254. <https://doi.org/10.1016/j.tics.2013.03.003>.
- Chen, C.H., Fremont, R., Arteaga-Bracho, E.E., and Khodakhah, K. (2014). Short latency cerebellar modulation of the basal ganglia. *Nat. Neurosci.* 17, 1767–1775. <https://doi.org/10.1038/nn.3868>.
- Cui, G., Jun, S.B., Jin, X., Pham, M.D., Vogel, S.S., Lovinger, D.M., and Costa, R.M. (2013). Concurrent activation of striatal direct and indirect pathways during action initiation. *Nature* 494, 238–242. <https://doi.org/10.1038/nature11846>.
- Cunningham, J.P., and Yu, B.M. (2014). Dimensionality reduction for large-scale neural recordings. *Nat. Neurosci.* 17, 1500–1509. <https://doi.org/10.1038/nn.3776>.
- DeLong, M.R. (1990). Primate models of movement disorders of basal ganglia origin. *Trends Neurosci.* 13, 281–285. [https://doi.org/10.1016/0166-2236\(90\)90110-V](https://doi.org/10.1016/0166-2236(90)90110-V).
- Eriksson, S., Lasic, S., and Topgaard, D. (2013). Isotropic diffusion weighting in PGSE NMR by magic-angle spinning of the q-vector. *J. Magn. Reson.* 226, 13–18. <https://doi.org/10.1016/j.jmr.2012.10.015>.
- Foster, N.N., Barry, J., Korobkova, L., Garcia, L., Gao, L., Becerra, M., Sherfat, Y., Peng, B., Li, X., Choi, J.-H., et al. (2021). The mouse cortico-basal ganglia-thalamic network. *Nature* 598, 188–194. <https://doi.org/10.1038/s41586-021-03993-3>.

- Freeze, B.S., Kravitz, A.V., Hammack, N., Berke, J.D., and Kreitzer, A.C. (2013). Control of basal ganglia output by direct and indirect pathway projection neurons. *J. Neurosci.* 33, 18531–18539. <https://doi.org/10.1523/jneurosci.1278-13.2013>.
- Friedman, A., Homma, D., Gibb, G., Leif, Amemori, K.-I., Rubin, J., Samuel, Hood, S., Adam, Riad, H., Michael, and Graybiel, M. (2015). A corticostriatal path targeting striosomes controls decision-making under conflict. *Cell* 161, 1320–1333. <https://doi.org/10.1016/j.cell.2015.04.049>.
- Friston, K., Harrison, L., and Penny, W. (2003). Dynamic causal modelling. *Neuroimage* 19, 1273–1302. [https://doi.org/10.1016/S1053-8119\(03\)00202-7](https://doi.org/10.1016/S1053-8119(03)00202-7).
- Frässle, S., Aponte, E., Bollmann, S., Brodersen, K., Do, C., Harrison, O., Harrison, S., Heinze, J., Iglesias, S., Kasper, L., et al. (2021). TAPAS: an open-source software package for translational neuromodeling and computational psychiatry. *Front. Psychiatry* 12, 680811. <https://doi.org/10.3389/fpsy.2021.680811>.
- Frässle, S., Lomakina, E.I., Kasper, L., Manjaly, Z.M., Leff, A., Pruessmann, K.P., Buhmann, J.M., and Stephan, K.E. (2018). A generative model of whole-brain effective connectivity. *Neuroimage* 179, 505–529. <https://doi.org/10.1016/j.neuroimage.2018.05.058>.
- Frässle, S., Lomakina, E.I., Razi, A., Friston, K.J., Buhmann, J.M., and Stephan, K.E. (2017). Regression DCM for fMRI. *Neuroimage* 155, 406–421. <https://doi.org/10.1016/j.neuroimage.2017.02.090>.
- Frässle, S., Manjaly, Z.M., Do, C.T., Kasper, L., Pruessmann, K.P., and Stephan, K.E. (2020). Whole-brain estimates of directed connectivity for human connectomics. *Neuroimage* 225, 117491. <https://doi.org/10.1016/j.neuroimage.2020.117491>.
- Gerfen, C., Engber, T., Mahan, L., Susel, Z., Chase, T., Monsma, F., and Sibley, D. (1990). D1 and D2 dopamine receptor-regulated gene expression of striatonigral and striatopallidal neurons. *Science (New York, N.Y.)* 250, 1429–1432. <https://doi.org/10.1126/science.2147780>.
- Gong, S., Doughty, M., Harbaugh, C.R., Cummins, A., Hatten, M.E., Heintz, N., and Gerfen, C.R. (2007). Targeting Cre recombinase to specific neuron populations with bacterial artificial chromosome constructs. *J. Neurosci.* 27, 9817–9823. <https://doi.org/10.1523/JNEUROSCI.2707-07.2007>.
- Gong, S., Zheng, C., Doughty, M.L., Losos, K., Didkovsky, N., Schambra, U.B., Nowak, N.J., Joyner, A., Leblanc, G., Hatten, M.E., and Heintz, N. (2003). A gene expression atlas of the central nervous system based on bacterial artificial chromosomes. *Nature* 425, 917–925. <https://doi.org/10.1038/nature02033>.
- Grissom, N.M., McKee, S.E., Schoch, H., Bowman, N., Havekes, R., O'Brien, W.T., Maht, E., Siegel, S., Commons, K., Portfors, C., et al. (2018). Male-specific deficits in natural reward learning in a mouse model of neurodevelopmental disorders. *Mol. Psychiatry* 23, 544–555. <https://doi.org/10.1038/mp.2017.184>.
- Hallett, M. (2011). Neurophysiology of dystonia: the role of inhibition. *Neurobiol. Dis.* 42, 177–184. <https://doi.org/10.1016/j.nbd.2010.08.025>.
- Hintiryan, H., Foster, N.N., Bowman, I., Bay, M., Song, M.Y., Gou, L., Yamashita, S., Bienkowski, M.S., Zingg, B., Zhu, M., et al. (2016). The mouse cortico-striatal projectome. *Nat. Neurosci.* 19, 1100–1114. <https://doi.org/10.1038/nn.4332>.
- Hoshi, E., Tremblay, L., Féger, J., Carras, P.L., and Strick, P.L. (2005). The cerebellum communicates with the basal ganglia. *Nat. Neurosci.* 8, 1491–1493. <https://doi.org/10.1038/nn1544>.
- Ichinohe, N., Mori, F., and Shoumura, K. (2000). A di-synaptic projection from the lateral cerebellar nucleus to the laterodorsal part of the striatum via the central lateral nucleus of the thalamus in the rat. *Brain Res.* 880, 191–197. [https://doi.org/10.1016/S0006-8993\(00\)02744-X](https://doi.org/10.1016/S0006-8993(00)02744-X).
- Ince, E., Ciliax, B., and Levey, A. (1997). Differential expression of D1 and D2 dopamine and m4 muscarinic acetylcholine receptor proteins in identified striatonigral neurons. *Synapse (New York, N.Y.)* 27. [https://doi.org/10.1002/\(SICI\)1098-2396\(199712\)27:4<357::AID-SYN9>3.0.CO;2-B](https://doi.org/10.1002/(SICI)1098-2396(199712)27:4<357::AID-SYN9>3.0.CO;2-B).
- Keilholz, S.D., Silva, A.C., Raman, M., Merkle, H., and Koretsky, A.P. (2006). BOLD and CBV-weighted functional magnetic resonance imaging of the rat somatosensory system. *Magn. Reson. Med.* 55, 316–324. <https://doi.org/10.1002/mrm.20744>.
- Kelly, R.M., and Strick, P.L. (2003). Cerebellar loops with motor cortex and prefrontal cortex of a nonhuman primate. *J. Neurosci.* 23, 8432–8444. <https://doi.org/10.1523/jneurosci.23-23-08432.2003>.
- Kravitz, A.V., Freeze, B.S., Parker, P.R., Kay, K., Thwin, M.T., Deisseroth, K., and Kreitzer, A.C. (2010). Regulation of Parkinsonian motor behaviours by optogenetic control of basal ganglia circuitry. *Nature* 466, 622–626. <https://doi.org/10.1038/nature09159>.
- Kreitzer, A.C., and Malenka, R.C. (2007). Endocannabinoid-mediated rescue of striatal LTD and motor deficits in Parkinson's disease models. *Nature* 445, 643–647. <https://doi.org/10.1038/nature05506>.
- Kumar, V., Grissom, N., McKee, S., Schoch, H., Bowman, N., Havekes, R., Kumar, M., Pickup, S., Poptani, H., Reyes, T., et al. (2018). Linking spatial gene expression patterns to sex-specific brain structural changes on a mouse model of 16p11.2 hemideletion. *Transl. Psychiatry* 8, 109. <https://doi.org/10.1038/s41398-018-0157-z>.
- Leblanc, K.H., London, T.D., Szczot, I., Bocarsly, M.E., Friend, D.M., Nguyen, K.P., Mengesha, M.M., Rubinstein, M., Alvarez, V.A., and Kravitz, A.V. (2020). Striatopallidal neurons control avoidance behavior in exploratory tasks. *Mol. Psychiatry* 25, 491–505. <https://doi.org/10.1038/s41380-018-0051-3>.
- Lee, H.J., Weitz, A.J., Bernal-Casas, D., Duffy, B.A., Choy, M., Kravitz, A.V., Kreitzer, A.C., and Lee, J.H. (2016). Activation of direct and indirect pathway medium spiny neurons drives distinct brain-wide responses. *Neuron* 91, 412–424. <https://doi.org/10.1016/j.neuron.2016.06.010>.
- Lee, S.P., Silva, A.C., Ugurbil, K., and Kim, S.G. (1999). Diffusion-weighted spin-echo fMRI at 9.4 T: microvascular/tissue contribution to BOLD signal changes. *Magn. Reson. Med.* 42, 919–928. [https://doi.org/10.1002/\(sici\)1522-2594\(199911\)42:5<919::aid-mrm12>3.0.co;2-8](https://doi.org/10.1002/(sici)1522-2594(199911)42:5<919::aid-mrm12>3.0.co;2-8).
- Loewke, A., Minerva, A., Nelson, A., Kreitzer, A., and Gunaydin, L. (2021). Frontostriatal projections regulate innate avoidance behavior. *J. Neurosci.* 41, 5487–5501. <https://doi.org/10.1523/JNEUROSCI.2581-20.2021>.
- Mathis, A., Mamidanna, P., Cury, K.M., Abe, T., Murthy, V.N., Mathis, M.W., and Bethge, M. (2018). DeepLabCut: markerless pose estimation of user-defined body parts with deep learning. *Nat. Neurosci.* 21, 1281–1289. <https://doi.org/10.1038/s41593-018-0209-y>.
- Middleton, F.A., and Strick, P.L. (2001). Cerebellar projections to the prefrontal cortex of the primate. *J. Neurosci.* 21, 700–712.
- Nunes, D., Gil, R., and Shemesh, N. (2021). A rapid-onset diffusion functional MRI signal reflects neuromorphological coupling dynamics. *Neuroimage* 237, 117862. <https://doi.org/10.1016/j.neuroimage.2021.117862>.
- Nunes, D., Ianus, A., and Shemesh, N. (2019). Layer-specific connectivity revealed by diffusion-weighted functional MRI in the rat thalamocortical pathway. *Neuroimage* 184, 646–657. <https://doi.org/10.1016/j.neuroimage.2018.09.050>.
- Oh, S.W., Harris, J.A., Ng, L., Winslow, B., Cain, N., Mihalas, S., Wang, Q., Lau, C., Kuan, L., Henry, A.M., et al. (2014). A mesoscale connectome of the mouse brain. *Nature* 508, 207–214. <https://doi.org/10.1038/nature13186>.
- Oorschot, D.E. (2010). Cell types in the different nuclei of the basal ganglia. In *Handbook of Behavioral Neuroscience* (Elsevier), pp. 63–74. <https://doi.org/10.1016/b978-0-12-374767-9.00003-2>.
- Pan, W.X., Mao, T., and Dudman, J.T. (2010). Inputs to the dorsal striatum of the mouse reflect the parallel circuit architecture of the forebrain. *Front. Neuroanat.* 4, 147. <https://doi.org/10.3389/fnana.2010.00147>.
- Penny, W., Stephan, K., Daunizeau, J., Rosa, M., Friston, K., Schofield, T., and Leff, A. (2010). Comparing families of dynamic causal models. *PLoS Comput. Biol.* 6, e1000709. <https://doi.org/10.1371/journal.pcbi.1000709>.
- Penny, W.D., Stephan, K.E., Mechelli, A., and Friston, K.J. (2004). Comparing dynamic causal models. *Neuroimage* 22, 1157–1172. <https://doi.org/10.1016/j.neuroimage.2004.03.026>.

- Peters, A.J., Steinmetz, N.A., Harris, K.D., and Carandini, M. (2019). Striatal activity reflects cortical activity patterns. *Nature* 591, 420–425. <https://doi.org/10.1101/703710>.
- Portmann, T., Yang, M., Mao, R., Panagiotakos, G., Ellegood, J., Dolen, G., Bader, P., Grueter, B., Goold, C., Fisher, E., et al. (2014). Behavioral abnormalities and circuit defects in the basal ganglia of a mouse model of 16p11.2 deletion syndrome. *Cell Rep.* 7, 1077–1092. <https://doi.org/10.1016/j.celrep.2014.03.036>.
- Posner, M.I., Rothbart, M.K., Sheese, B.E., and Tang, Y. (2007). The anterior cingulate gyrus and the mechanism of self-regulation. *Cogn. Affective, Behav. Neurosci.* 7, 391–395. <https://doi.org/10.3758/cabn.7.4.391>.
- Ridderinkhof, K.R., Ullsperger, M., Crone, E.A., and Nieuwenhuis, S. (2004). The role of the medial frontal cortex in cognitive control. *Science* 306, 443–447. <https://doi.org/10.1126/science.1100301>.
- Simonyan, K., Berman, B.D., Herscovitch, P., and Hallett, M. (2013). Abnormal striatal dopaminergic neurotransmission during rest and task production in spasmodic dysphonia. *J. Neurosci.* 33, 14705–14714. <https://doi.org/10.1523/JNEUROSCI.0407-13.2013>.
- Simonyan, K., Cho, H., Hamzehei Sichani, A., Rubien-Thomas, E., and Hallett, M. (2017). The direct basal ganglia pathway is hyperfunctional in focal dystonia. *Brain* 140, 3179–3190. <https://doi.org/10.1093/brain/awx263>.
- Snyder, H.R., Kaiser, R.H., Warren, S.L., and Heller, W. (2015a). Obsessive-compulsive disorder is associated with broad impairments in executive function. *Clin. Psychol. Sci.* 3, 301–330. <https://doi.org/10.1177/2167702614534210>.
- Snyder, H.R., Miyake, A., and Hankin, B.L. (2015b). Advancing understanding of executive function impairments and psychopathology: bridging the gap between clinical and cognitive approaches. *Front. Psychol.* 6, 328. <https://doi.org/10.3389/fpsyg.2015.00328>.
- Sturman, O., von Ziegler, L., Schläppli, C., Akyol, F., Privitera, M., Slominski, D., Grimm, C., Thieren, L., Zerbi, V., Grewe, B., and Bohacek, J. (2020). Deep learning-based behavioral analysis reaches human accuracy and is capable of outperforming commercial solutions. *Neuropsychopharmacology* 45, 1942–1952. <https://doi.org/10.1038/s41386-020-0776-y>.
- Tononi, G., Sporns, O., and Edelman, G.M. (1999). Measures of degeneracy and redundancy in biological networks. *Proc. Natl. Acad. Sci. U S A.* 96, 3257–3262. <https://doi.org/10.1073/pnas.96.6.3257>.
- Topgaard, D. (2017). Multidimensional diffusion MRI. *J. Magn. Reson.* 275, 98–113. <https://doi.org/10.1016/j.jmr.2016.12.007>.
- Zhang, J., Zhang, L., Jiao, H., Zhang, Q., Zhang, D., Lou, D., Katz, J.L., and Xu, M. (2006). c-Fos facilitates the acquisition and extinction of cocaine-induced persistent changes. *J. Neurosci.* 26, 13287–13296. <https://doi.org/10.1523/jneurosci.3795-06.2006>.
- Zhao, F., Wang, P., and Kim, S.G. (2004). Cortical depth-dependent gradient-echo and spin-echo BOLD fMRI at 9.4T. *Magn Reson Med* 51, 518–524. <https://doi.org/10.1002/mrm.10720>.

## STAR★METHODS

### KEY RESOURCES TABLE

REAGENT or RESOURCE	SOURCE	IDENTIFIER
<b>Antibodies</b>		
Rabbit anti-cFos	Synaptic Systems	Cat#226 003; RRID: AB_2231974
Goat anti-rabbit Alexa 546	Thermo Fisher Scientific	Cat#A-11035; RRID: AB_2534093
<b>Bacterial and virus strains</b>		
AAV-5/2-hEF1 $\alpha$ -dlox-hChr2(H134R)_EYFP(rev)-dlox-WPRE-hGHp(A)	Viral Vector Facility (VVF)	VVF Repository: v214-5
AAV-5/2-hSyn-dlox-EYFP(rev)-dlox-WPRE-hGHp(A)	Viral Vector Facility (VVF)	VVF Repository: V115-5
<b>Chemicals, peptides, and recombinant proteins</b>		
Pancuronium bromide	Sigma-Aldrich	Cat#P1918
Isoflurane (Attane)	Piramal Healthcare Limited	Swissmedic #56761
Midazolam	Neuraxpharm Switzerland AG, Switzerland	Swissmedic #62556
Medetomidin	Orion Pharma, Finland	Swissmedic #50590
Fentanyl	Sintetica SA, Switzerland	Swissmedic #53987
Temgesic	Indivior Schweiz AG, Switzerland	Swissmedic #41931
Antisedan	Orion Pharma, Finland	Swissmedic #50819
Anexate	CPS Cito Pharma Services GmbH, Switzerland	Swissmedic #48280
Permaplast LH Flow, dental cement	M+W Dental, Switzerland	Cat #100106
Etching gel	DMG, Germany	Cat #198178
<b>Deposited data</b>		
Allen Reference Atlas	<a href="http://mouse.brain-map.org/static/atlas">http://mouse.brain-map.org/static/atlas</a>	RRID:SCR_013286
Allen Mouse Brain Atlas (AMBA)	<a href="http://mouse.brain-map.org/">http://mouse.brain-map.org/</a>	RRID:SCR_002978
<b>Experimental models: Organisms/strains</b>		
B6.FVB(Cg)-Tg(Drd1-cre)EY262Gsat/Mmucd	(Gong et al., 2003)	MGI:3836631
B6.FVB(Cg)-Tg(Drd2-cre)ER44Gsat/Mmucd	(Gong et al., 2003)	MGI:3836635
B6.FVB(Cg)-Tg(Adora2a-cre)KG139Gsat/Mmucd	(Gong et al., 2003); Laboratory of Prof. Denis Burdakov	MGI:4361654
<b>Software and algorithms</b>		
MATLAB	MathWorks	RRID:SCR_001622
FSL	Analysis Group, FMRIB, Oxford, UK	RRID:SCR_002823
ANTS (Advanced Normalization Tools)	<a href="http://picsl.upenn.edu/software/ants/">http://picsl.upenn.edu/software/ants/</a>	RRID:SCR_004757
TAPAS	(Frässle et al., 2021); <a href="https://www.tnu.ethz.ch/de/software/tapas">https://www.tnu.ethz.ch/de/software/tapas</a>	N/A
DLCAnalyzer in DeepLabCut 2.0.7 (python toolbox)	(Frässle et al., 2021; Sturman et al., 2020); <a href="https://github.com/ETHZ-INS/DLCAnalyzer">https://github.com/ETHZ-INS/DLCAnalyzer</a>	RRID:SCR_008394
COSplay trigger	(Aymanns et al., 2020); <a href="https://cosplay.readthedocs.io/en/latest/">https://cosplay.readthedocs.io/en/latest/</a>	N/A

### RESOURCE AVAILABILITY

#### Lead contact

Further information and requests for resources and reagents should be directed to and will be fulfilled by the lead contact, Valerio Zerbi ([valerio.zerbi@hest.ethz.ch](mailto:valerio.zerbi@hest.ethz.ch)).



### Materials availability

This study did not generate new unique reagents.

### Data and code availability

All data reported in this paper will be shared by the lead contact upon request.

This paper does not report original code.

Any additional information required to reanalyze the data reported in this paper is available from the lead contact upon request.

## EXPERIMENTAL MODELS AND SUBJECT DETAILS

### Animals

All animal procedures were conducted in accordance with the Swiss Federal Ordinance on Animal Experimentation and approved by the Cantonal Veterinary Office of Zurich. Experiments were performed using three inbred BAC-mediated transgenic mouse lines from GENSAT (Gong et al., 2003) aged 8 to 12 weeks: B6.FVB(Cg)-Tg(Drd1-cre)EY262Gsat/Mmucd (in-house breeding), B6.FVB(Cg)-Tg(Drd2-cre)ER44Gsat/Mmucd (in-house breeding) and B6.FVB(Cg)-Tg(Adora2a-cre)KG139Gsat/Mmucd (generously provided by Prof. Denis Burdakov). Male and female D1-Cre (n(male)=5; n(female)=9), D2-Cre (n(male)=4; n(female)=4) and A2A-Cre (n(male)=6, n(female)=7) were maintained in IVC cages and housed in groups of 2-5 mice per cage. Food and water were provided *ad libitum* in a temperature- and humidity-controlled facility on a 12h light/dark cycle. Behavioural experiments were conducted one week prior to opto-fMRI recordings. For behavioural experiments, 9 male and female D1-Cre and 8 male and female D2-Cre mice were used. For opto-fMRI recordings, 11 male and female D1-Cre and 8 male and female D2-Cre mice were used.

## METHOD DETAILS

### Stereotaxic surgery

Viral vectors were obtained from the Viral Vector Facility (VVF) of the Neuroscience Center Zurich. Experimental D1-, D2- and A2A-Cre mice were injected unilaterally with 300 nl of an AAV viral construct (AAV5-hEF1 $\alpha$ -dlox-hChR2(H134R)-EYFP(rev)-dlox-WPRE-hGHp(A); titer:  $6.3 \times 10^{12}$  vector genomes/ml). Control mice (D1-Cre) were injected with 300 nl of a fluorophore-only carrying AAV construct (AAV5-hSyn-dlox-EYFP(rev)-dlox-WPRE-hGHp(A); titer:  $6.3 \times 10^{12}$  vector genomes/ml). Stereotaxic surgery was performed under anesthesia with a mixture of midazolam (5mg/ml; Neuraxpharm Switzerland AG, Switzerland), fentanyl (50mcg/ml; Sintetica SA, Switzerland) and medetomidine (1mg/ml; Orion Pharma, Finland). Animals were placed into a stereotaxic apparatus (Neurostar, Germany) and their skulls exposed. Etching gel (DMG, Germany) was applied to the air-dried skull for 30 seconds and the bone surface was gently scratched using a metal scaler. After removal of bone debris with saline, bregma was located and the skull placement corrected for tilt and scaling. For virus delivery and optical fiber implantation in the ventrolateral striatum a small hole was drilled at AP -0.1, ML -2.6, DV 3.7 relative to bregma. Following virus delivery, an optical fiber bent to a 90-degree angle (400 $\mu$ m, NA=0.66; laser light transmission: 60%; Doric Lenses, Canada) was placed at 0.2 mm above the targeted site and glued to the skull using a UV-curable dental composite (Permaplast, LH Flow; M+W Dental, Switzerland). Stitches were placed as required. Laser light transmission of each 90 degree bent optical fiber, optimized to fit the high SNR cryogenic MRI coil, was assessed before implantation to reach 3.0 to 3.5 mW illumination intensity at the fiber tip. Throughout the surgical procedure, body temperature was kept at 35 °C using a heating pad (Harvard Apparatus, USA). Following implantation, an anesthesia antidote mixture containing temgesic (0.3mg/ml; Indivior Schweiz AG, Switzerland), annexate (0.1mg/ml; CPS Cito Pharma Services GmbH, Switzerland), antisedan (0.1mg/ml; Orion Pharma, Finland) was administered subcutaneously and mice were placed into a heating chamber to recover. All animals were monitored for 3 days after surgery and left to recover for 3 - 4 weeks before behavioural and scanning sessions.

### Open-field test in freely moving mice

Behavioural testing took place in a dimly lit chamber with sound insulating properties. Laser-light evoked changes in rotational behaviour of experimental D1- and D2- Cre mice (Gong et al., 2007; Zhang et al., 2006) were quantified during an open-field test. Animals were placed in a 40 x 40 cm arena and left to explore freely for 15 minutes. After this habituation period, mice were subjected to five cycles of 20s laser stimulation at 473 nm and 20 Hz (ON) with 3.0 to 3.5 mW laser power followed by 40s of no laser stimulation (OFF). Motor behaviour was video recorded at all times.

### Opto-fMRI recording

#### Animal preparation

For fMRI data acquisition, mice were anesthetized in a gas chamber for 4 minutes with 4% isoflurane in 1:4 O<sub>2</sub> to air mixture. Animals were endotracheally intubated and the tail vein cannulated while being kept under anesthesia with 2% isoflurane. During preparation, animal temperature was kept at 35 °C using a heating pad (Harvard Apparatus, USA). Once intubated and cannulated, mice were

head-fixed with earbars and connected to a small animal ventilator (CWE, Ardmore, USA) on an MRI-compatible support. Ventilation was set to 80 breaths per minute, with 1.8 ml/min flow with isoflurane at 2%. A bolus containing a mixture of medetomidine (0.05mg/kg) and pancuronium (0.25mg/kg) was delivered via the cannulated vein. Isoflurane was set to 1.5%. Continuous infusion of medetomidine (0.1mg/kg/h) and pancuronium (0.25mg/kg/h) started five minutes after the initial bolus injection. Isoflurane was reduced to 0.5% to minimize its accumulative effects and avoid too deep of a sedation. As an additional measure to control for anesthesia depth, a 36 °C hot water-circulation bed kept the temperature of the animal constant throughout the entire measurement. Stable body temperature was monitored via a rectal temperature probe. After collection of functional and anatomical fMRI scans continuous injection and isoflurane flow were stopped. Animals remained connected to the ventilator until independent breathing could be assured. For further recovery, they were transferred to a heating chamber.

#### Data acquisition

Data were acquired in a 7T Bruker BioSpec scanner equipped with a Pharmascan magnet and a high SNR dedicated mouse brain cryogenic coil (Bruker BioSpin AG, Fällanden, Switzerland). For each experimental mouse, we acquired three different modalities of functional acquisition in two fMRI scanning sessions. Gradient-echo (GE) and Spin-echo (SE) sequences were acquired to capture BOLD contrast via T2\* and T2 weighted signals. In addition, we implemented isotropic diffusion encoding (IDE) gradient waveforms to impart a diffusion weighting functional contrast as in (Eriksson et al., 2013; Topgaard, 2017). Control mice were scanned using the GE BOLD fMRI sequence only. For GE BOLD fMRI, an echo planar imaging sequence (EPI, repetition time TR = 1000 ms, total volumes = 480, slice thickness ST = 0.45 mm, in-plane spatial resolution RES = 0.22×0.2 mm<sup>2</sup>) was used to collect 2 to 4 datasets from each mouse. For SE sequences (including the IDE gradient waveforms implementation for diffusion weighting), 4 datasets were acquired in each mouse within a single session. For diffusion-weighted fMRI (dfMRI), a SE EPI sequence was used (TR = 1000 ms, total volumes = 480, ST = 1.45 mm, RES = 0.23×0.23 mm<sup>2</sup>, b = 1500 s/mm<sup>2</sup>). To impart BOLD contrast, this sequence was used as is (i.e. b = 0 s/mm<sup>2</sup>), given it delivers T<sub>2</sub> - weighted signals (Nunes et al., 2019). For both SE and dfMRI sequences, EPI slices were positioned according to anatomy, capturing the entire midbrain and part of the PFC (bregma +1.33). Anatomical scans were acquired via a FLASH sequence with an in-plane resolution of 0.05 × 0.02 mm<sup>2</sup>, an echo time (TE) of 3.51 ms and a repetition time (TR) of 522 ms.

#### Optogenetic stimulation

Experimental and control mice were light stimulated via an optical fiber (Doric Lenses, Canada) connected to a custom-made DPSS laser (CNI laser, China). Following a baseline period of 170 seconds, trains of 473 nm laser pulses were delivered at 20 Hz and 3.0 to 3.5 mW for 20 seconds (ON) followed by 40 seconds of no laser light delivery (OFF) repeated over five minutes. The precise onset of laser pulses was controlled using the COSplay trigger device (Aymanns et al., 2020). To mitigate the visual artifacts of 'spilling' blue laser light, an additional light source in the form of an LED lamp was placed on the cradle inside the scanner.

#### Tissue collection for immunohistochemistry

Tissue collection for immunohistochemistry was performed at 90 min following a 3 min continuous 20 Hz optogenetic stimulation at 473 nm and 3.0 to 3.5 mW. Animals were deeply anesthetized with a ketamine/xylazine/acepromazine (100 mg/mL, 20 mg/mL, 10 mg/mL) mixture and intracardially perfused using 20 mL ice-cold PBS (pH 7.4). Brain tissue was fixated with an intracardial perfusion of ice-cold 4% PFA. The brain was dissected, post-fixated in 4% PFA at 4°C for 1 hour, rinsed with PBS and transferred to a sucrose solution (30% sucrose in PBS) to be stored at 4°C overnight. Once fully dehydrated, the brain was frozen in tissue mounting medium (Tissue-Tek O.C.T Compound, Sakura Finetek Europe B.V., Netherlands) and coronally sectioned into 40 µm thick slices using a cryostat (Leica CM3050 S, Leica Biosystems Nussloch GmbH). Brain sections were transferred to ice-cold PBS for further immunohistochemical processing.

#### Immunohistochemistry

For immunohistochemistry, brain slices were submerged in a primary antibody solution of 0.2% Triton X-100 and 2% normal goat serum in PBS. Sections were incubated under continuous agitation at 4°C for 2 nights. After washing 3 times/10 minutes in PBS, sections were transferred to incubate in secondary antibody solution for 1 hour at room temperature. Brain sections were washed 3 times/10 minutes, mounted onto glass slides (Menzel-Gläser SUPERFROST PLUS, Thermo Scientific) and air-dried before cover-slipping with Dako fluorescence mounting medium (Agilent Technologies). Antibodies included rabbit anti-pre-pro-enkephalin (ppENK; 1:200, Neuromics Cat# RA14124 RRID:AB\_2532106) with secondary antibody Alexa Fluor® 546 goat anti-rabbit (A11035, Life Technologies, 1:300), rabbit anti-cFos (226 003, Synaptic Systems, 1:5000) with secondary antibody Alexa 546 goat anti-rabbit (A11035, Life Technologies, 1:300), rabbit anti-prodynorphin (PA5-96439, Thermo Fisher Scientific, 1:200) with secondary antibody Alexa Fluor® 546 goat anti-rabbit (A11035, Life Technologies, 1:300), and Nissl stain (N21483, NeuroTrace 640/660 Nissl stain, Thermo Fisher Scientific, 1:300). Opsin and cFos expression were validated using a confocal laser-scanning microscope (CLSM 880, Carl Zeiss AG, Germany).

#### QUANTIFICATION AND STATISTICAL ANALYSIS

Statistical details for every experiment are provided in the figure legends, where "n" represents number of animals per group. Statistical significance was defined as p < 0.05.

### Open-field test in freely moving mice

Head angle tracking in freely moving, experimental mice was performed with the python toolbox DeepLabCut 2.0.7 (Mathis et al., 2018) using 13 body points of interest and 4 landmark points of interest within the open field arena. The network was trained using 10–20 frames from randomly selected videos for 250'000 – 1'030'000 iterations. The data generated by DeepLabCut was processed using custom R scripts (available online at <https://github.com/ETHZ-INS/DLCAnalyzer>) (Sturman et al., 2020).

### GLM statistical mapping

Preprocessing and functional data analysis was carried out using FSL FEAT (version 5.92, [www.fmrib.ox.ac.uk/fsl](http://www.fmrib.ox.ac.uk/fsl)) and in-house Matlab scripts. Pre-statistical processing included the following steps: Pre-processing of the BOLD data included discarding the first ten measurements to ensure achieving steady-state excitation, high pass filtering (with a cut-off of 90s), motion correction using MCFLIRT, spatial smoothing using a Gaussian kernel of FWHM 0.4 mm and interleaved slice timing correction. To account for potential alignment artifacts due to the implanted optical fiber, two study-specific templates based on all mean-EPIs and T1-weighted anatomical images were created using Advanced Normalization Tools (ANTs, <http://stnava.github.io/ANTs/>). Registration was first carried out to the respective T1-weighted image and then to the study-specific standard space template, using FLIRT and FNIRT. Subsequently, quality of alignment and normalization of each subject was visually inspected. Time series statistical analysis was carried out using FILM with local autocorrelation correction. First-level (time series) parameter estimates were computed using a voxel-based general linear model based on the gaussian hemodynamic response function, its temporal derivatives, and standard motion parameters (MCFLIRT). Group-level analysis was performed using FMRIB's Local Analysis of Mixed Effects (FLAME). An averaged whole-brain map was created for the v1 CPU's laser stimulation ON versus laser stimulation OFF contrast. In a third step, whole-brain differences between groups were tested (group contrast activation). Z-statistic images were thresholded using clusters determined by  $z > 3.1$ , and a familywise error-corrected cluster significance threshold of  $p < 0.05$  was applied to the suprathreshold clusters.

For visualization purposes, averaged group and group contrast activation maps were normalized to a high-resolution Allen Brain Institute (ABI) anatomical atlas using a greedy transformation.

### Dimensionality reduction

To visualize the dynamics of whole-brain BOLD changes evoked by D1R and D2R cell activation, we projected our BOLD-fMRI data onto a low-dimensional space. Briefly, time-varying BOLD signals were averaged across conditions and converted to a 2D matrix of [voxel \* time]. This matrix was then fed into an unsupervised manifold learning technique (Uniform Manifold Approximation and Projection, UMAP), which preserves the global data structure and local relationships with neighbours. Point-to-point distances in the UMAP plots were then used to interpret the continuity (or discontinuity) of the fMRI activity patterns and to identify similarities in temporal and spatial profiles between individual stimulations (Becht et al., 2018).

### rDCM analysis

Anatomical regions of interest (ROIs) for the regression dynamic causal modeling (rDCM) analysis were selected using an in-house Matlab script. In short, local activation maxima and minima (connected components of voxels) in D1- and D2-Cre group z-stat maps (experimental groups) were identified via an imposed upper and lower threshold (top and bottom 2%). Once thresholded, pixel connectivity was set to a 6-connected neighbourhood and finally transformed into unique clusters of regional maxima/minima. From D1- and D2-Cre group z-stat maps, a total of 30 clusters were identified and anatomically labelled: anterior cingulate (ACAv, 784 voxels); infralimbic area (IL, 629 voxels); agranular insula dorsal/ventral (Ald/Alv, 571 voxels); primary motor cortex (MOp, 446 voxels); primary somatosensory cortex, mouth area (SSp-m, 2159 voxels); primary somatosensory cortex, barrel field (SSp-bfd, 1411 voxels); gustatory area/claustum (GU/CLA, 1181 voxels); caudate putamen (CPu, 1104 voxels); bed nucleus of stria terminalis (BST, 452 voxels); anterior amygdalar area (AAA, 566 voxels); external globus pallidus (GPe, 610 voxels); internal globus pallidus (GPi, 259 voxels); sub-paraventricular zone (SBPV, 250 voxels); primary somatosensory cortex, lower limb (SSp-l, 378 voxels); visceral area (VISC, 78 voxels); temporal association area (TEa, 85 voxels); mediodorsal nucleus of thalamus (MD, 594 voxels); lateral amygdalar nucleus (LA, 337 voxels); medial amygdalar nucleus (MEA, 457 voxels); tuberal nucleus (TU, 527 voxels); ectorhinal area (ECT, 360 voxels); auditory area (AUD, 494 voxels); substantia nigra (SNr, 1226 voxels); medial mammillary nucleus, median part (Mmme, 311 voxels); cornu ammonis 3 (CA3, 1166 voxels); entorhinal area (ENT, 1211 voxels); inferior colliculus, external nucleus (ICe, 377 voxels); midbrain reticular nucleus (MRN, 246 voxels); simple lobule (SIM, 4313 voxels); Crus I (621 voxels). BOLD signal time series were then extracted as the average signal of all voxels within each cluster. Extracted time series entered effective (directed) connectivity analysis using rDCM.

For the rDCM analysis, we made use of the open-source rDCM toolbox, which is freely available as part of the TAPAS software package ([www.translationalneuromodeling.org/tapas](http://www.translationalneuromodeling.org/tapas)) (Frässle et al., 2021). In brief, rDCM is a variant of DCM for fMRI (Friston et al., 2003) that enables whole-brain effective connectivity analyses by reformulating the numerically costly estimation of coupling parameters in differential equations of a classical linear DCM in the time domain into an efficiently solvable Bayesian linear regression in the frequency domain (Frässle et al., 2018; Frässle et al., 2017).

Here, we applied two different strategies: First, we restricted ourselves to key components of the canonical BG-thalamocortical network: (i) MOp, (ii) CPu, (iii) GPe, (iv) GPi, (v) MD, and (vi) SNr. In a second step, we then assessed effective connectivity within a more extended brain-wide network that comprised 30 nodes, including cerebellar and prefrontal regions (among others).

For both analyses, we utilized the embedded sparsity constraints of rDCM to automatically prune connections without having to rely on *a priori* restrictions on network architecture (Frässle et al., 2018). In brief, sparsity is induced by introducing binary indicator variables as feature selectors into the likelihood function where each indicator variable determines whether a specific connectivity parameter is present or not. In other words, each connectivity parameter is multiplied with a binary variable that can be either 0 (indicating that the parameter is not important for explaining the data) or 1 (indicating that the parameter is essential for describing the data). Notably, a Bernoulli prior is specified on the binary indicator variables, where the Bernoulli distribution over the indicator variable associated with connection  $i$  is parameterized by a single parameter  $p_0^i$ . More precisely, subscript 0 indicates that  $p_0^i$  represents the parameter of a prior distribution (i.e., a hyperparameter), whereas superscript  $i$  represents the fact that  $p_0^i$  relates to a specific connection  $i$ . Intuitively,  $p_0^i$  encodes the *a priori* belief about the network's degree of sparseness.

Our rDCM analysis with sparsity constraints then initially assumed a fully (all-to-all) connected network, where all brain regions were coupled via reciprocal connections. Starting from this fully connected network, model inversion then automatically pruned connections to yield sparse effective connectivity patterns. Notably, since exact *a priori* knowledge about the degree of sparseness of the networks was not available, we followed previously established procedures for obtaining an optimal estimate of the network's sparseness  $p_0^i$  (Frässle et al., 2018). Specifically, for each mouse, we systematically varied  $p_0^i$  within a range of 0.1 to 0.9 in steps of 0.05 and performed model inversion for each  $p_0^i$  value. The optimal  $p_0^i$  value was then determined for each mouse by selecting the setting that yielded the highest log model evidence (as approximated by the negative free energy).

Importantly, to assess the construct validity of our approach in the present context, we tested whether rDCM could correctly identify the region that received the optogenetic stimulation (i.e. vl CPu). This is possible (and meaningful) because the present setting represents a rare case where 'ground truth' (i.e. the region that received the optogenetic stimulation) is known in an empirical dataset. We challenged rDCM to faithfully recover this ground truth by creating a model space comprising 6 models for the BG network analysis and 30 models for the full network analysis, respectively. Models differed in the region that received the driving input (i.e. optogenetic stimulation). Specifically, model 1 hypothesized region 1 (MOp) to receive the driving input, model 2 hypothesized region 2 (vl CPu) to receive the driving input, and so on. We then utilized fixed-effects Bayesian model selection (Penny et al., 2004) to compare the competing models based on their model evidence.

For the winning model, we then inspected the posterior parameter estimates by performing fixed-effects Bayesian averaging to obtain group posterior distributions over model parameters. Significance of parameter estimates was then assessed in terms of their posterior probability exceeding a threshold of 0.95 (Penny et al., 2010).

**Supplemental information**

**Optogenetic activation of striatal D1R and D2R**

**cells differentially engages downstream**

**connected areas beyond the basal ganglia**

**Christina Grimm, Stefan Frässle, Céline Steger, Lukas von Ziegler, Oliver Sturman, Noam Shemesh, Daria Peleg-Raibstein, Denis Burdakov, Johannes Bohacek, Klaas Enno Stephan, Daniel Razansky, Nicole Wenderoth, and Valerio Zerbi**



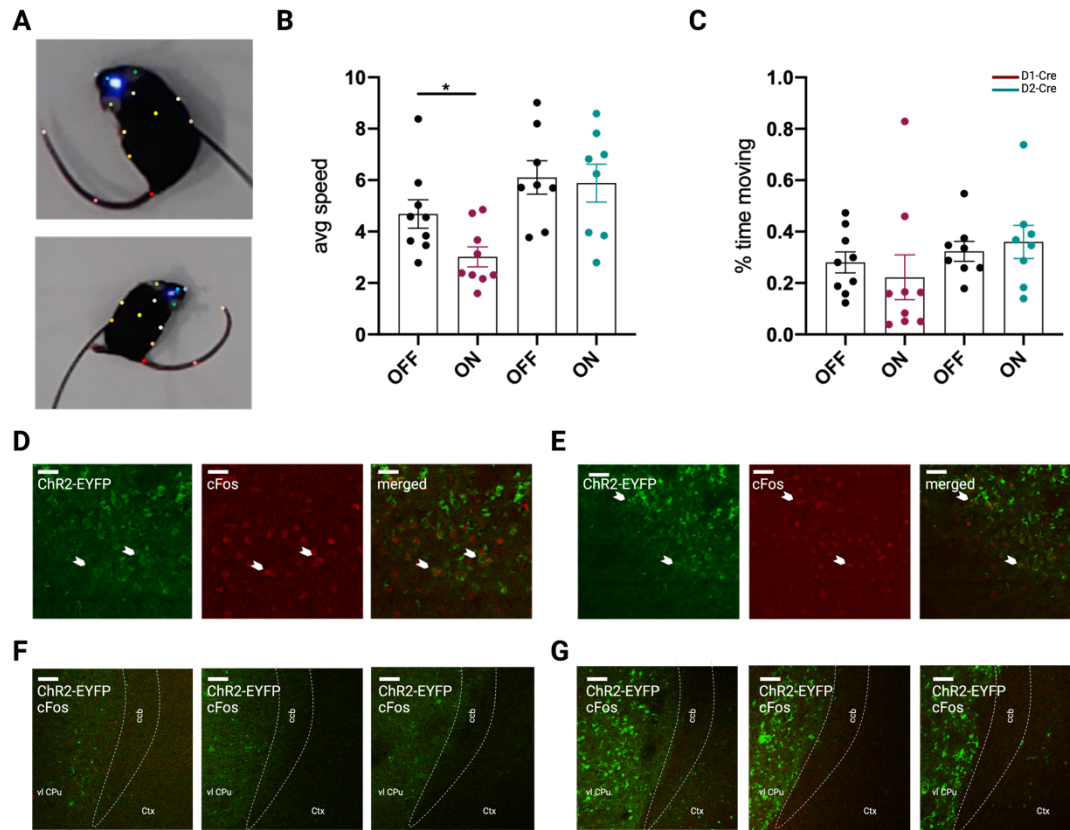


**Figure S1** Optogenetic stimulation of striatal D1R and D2R cells elicits changes at the behavioural and molecular level. Related to Figure 1. **A** Position of 13 body point labels for pose estimation using DeepLabCut. **B** Optogenetically evoked motor behaviour measured as changes in average speed. In D1-Cre mice, optogenetic stimulation significantly decreases average speed (\* $p = 0.03$ , linear mixed effects model with post hoc test), while no stimulation effect was detected in D2-Cre mice ( $p = 0.97$ , linear mixed effects model with post hoc test). **C** Optogenetically evoked motor behaviour measured as changes in percent of time moving. During optogenetic stimulation of striatal D1R and D2R cells no changes in the percent of time moving were detected ( $p(D1) = 0.55$ ,  $p(D2) = 0.64$ , linear mixed effects model with post hoc test). **D** Histological verification of ChR2 and cFos expression 90 min after sustained laser stimulation in vl CPu D1R cells. White arrowheads indicate representative cells co-expressing ChR2-EYFP and the stained antibody cFos. **E** Histological verification of ChR2 and cFos expression 90 min after sustained laser stimulation in vl CPu D2R cells. White arrowheads indicate representative cells co-expressing ChR2-EYFP and the stained antibody cFos. **F** Quantification of cFos expression in ChR2-EYFP D1-Cre mice. **G** Histological assessment of ChR2 and cFos expression in adjacent cortical region of D1-Cre mice. **H** Histological assessment of ChR2 and cFos expression in adjacent cortical region of D2-Cre mice. VI CPu, ventrolateral caudate putamen; ccb, corpus callosum, body; ctx, cortex. \*\* $p < 0.01$ , \*\*\* $p < 0.001$ . Scale bars, 50 $\mu$ m, 100 $\mu$ m.

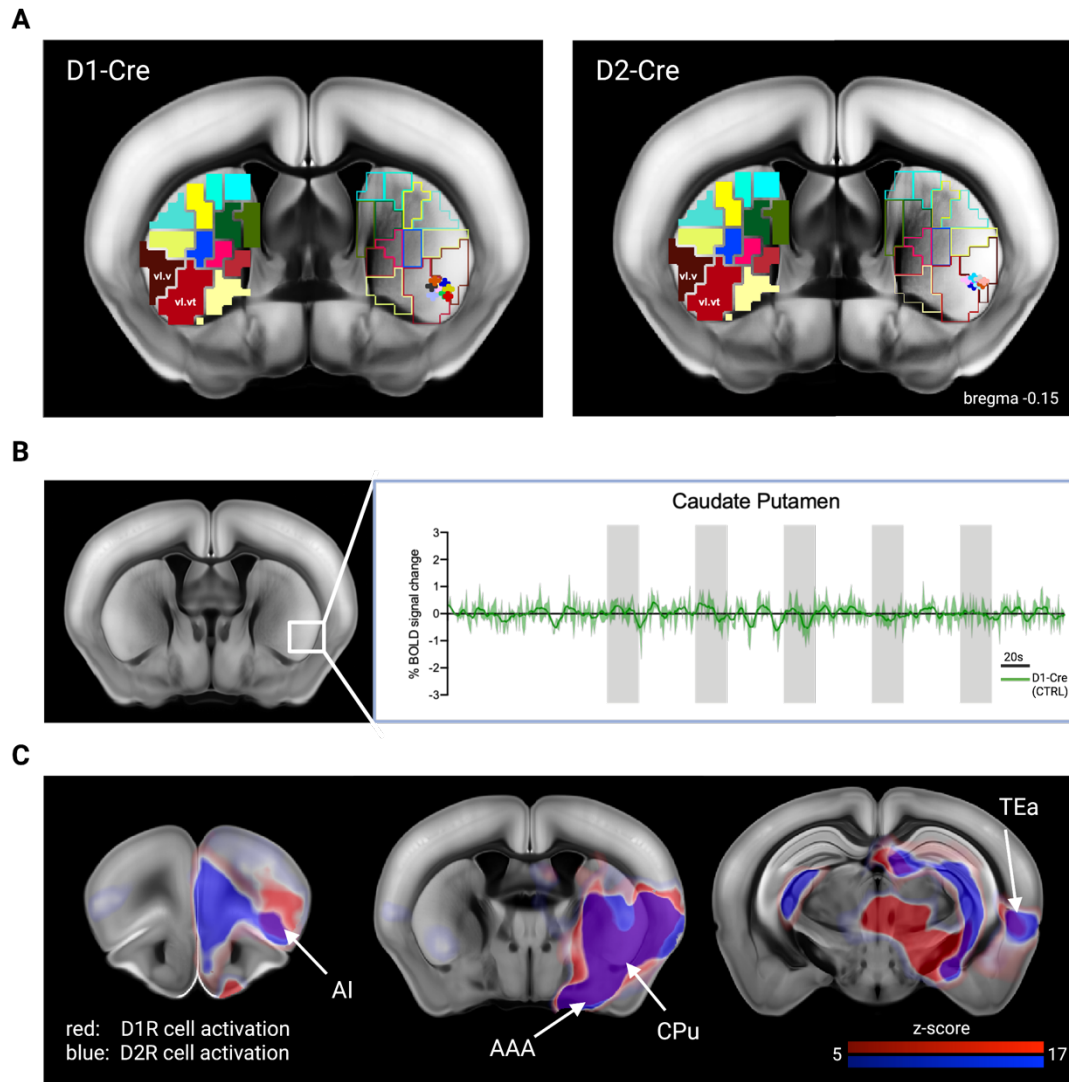


**Figure S2** Optogenetic stimulation of D1R and D2R cells in the ventrolateral CPu drives brain-wide activation and de-activation hotspots. Related to Figure 2. **A** Anatomical MRI verification of optical fiber placement in the vl CPu sub-region of D1- and D2-Cre mice. **B** Mean time-series extracted from the right vl CPu of control animals depicted in green ( $n(\text{D1}) = 3$  animals; no opsin expression). Laser stimulation blocks indicated in grey. **C** Overlay of thresholded D1 and D2 group z-stat activation maps, showing brain regions of similar BOLD signal profile. D1-Cre group z-stat activation map displayed in red color code, D2-Cre group z-stat activation map displayed in blue color code.  $N(\text{D1-Cre})=11$ ,  $n(\text{D2-Cre})=8$ . vl.v, ventrolateral-ventral; vl.vt, ventrolateral-ventral tip; AI, agranular insula; CPu, caudate putamen; AAA, anterior amygdalar area; TEa, temporal association area.

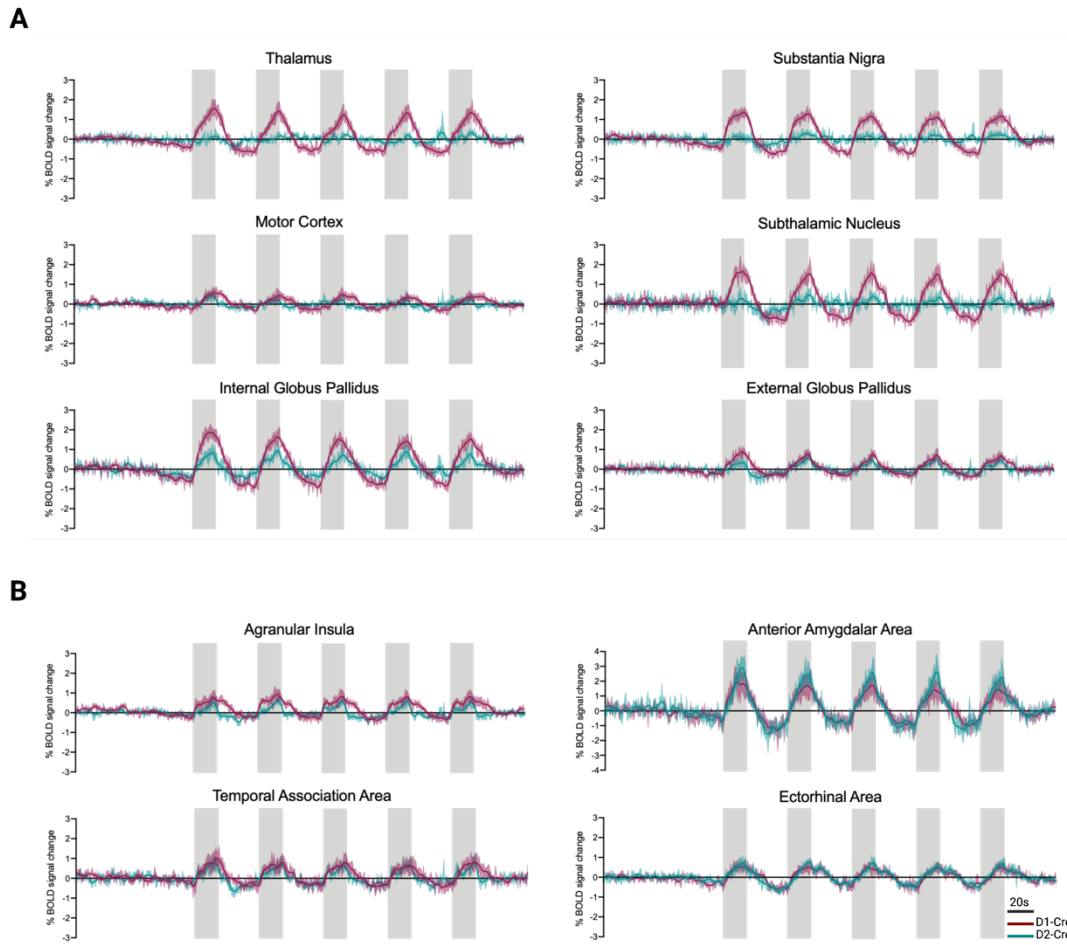


**Figure S3** Mean time-series of GE BOLD local activation maxima and minima. Related to Figure 2. **A** Mean time-series of D1-/D2-Cre mice extracted from selected BG regions of interest based on GE BOLD local activation maxima and minima z-stat maps. **B** Mean time-series of D1-/D2-Cre mice extracted from selected extra-BG regions of interest based on GE BOLD local activation maxima and minima z-stat maps. D1-Cre time-series depicted in maroon, D2-Cre time-series depicted in teal. Laser stimulation blocks indicated in grey.  $N(\text{D1-Cre})=11$ ,  $n(\text{D2-Cre})=8$ .

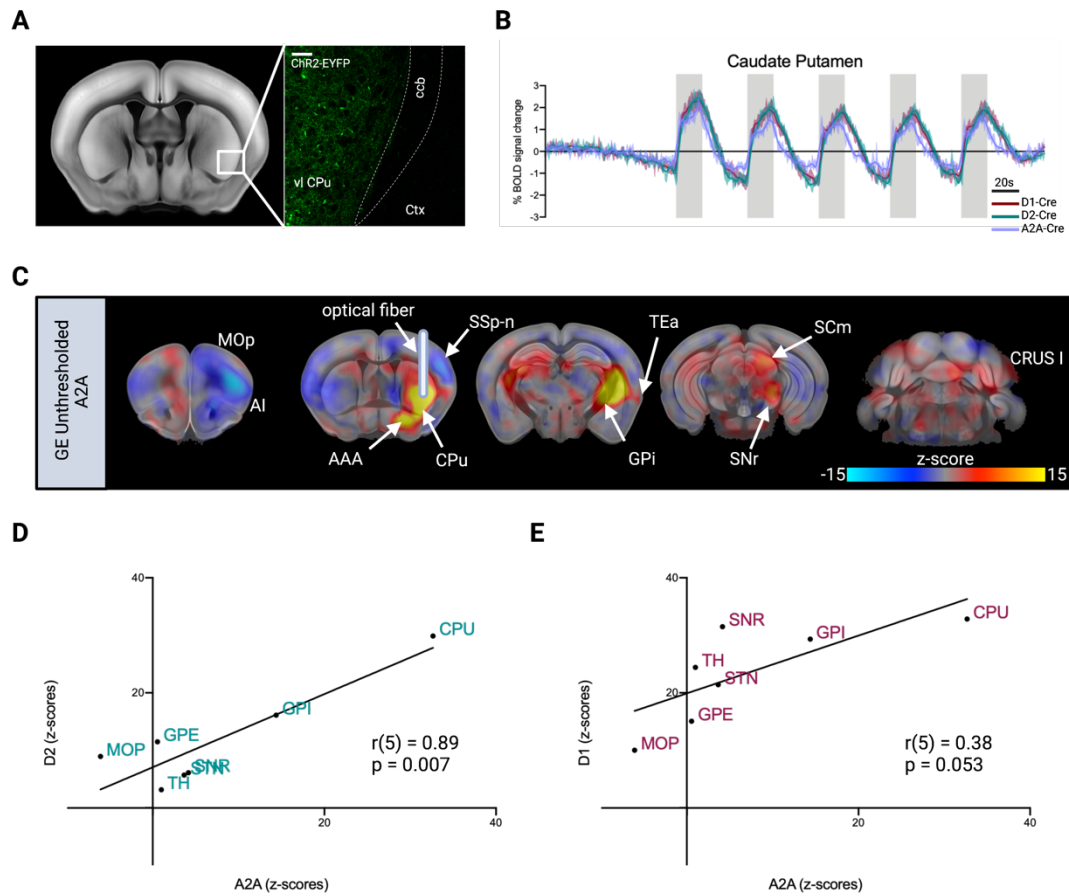


**Figure S4** D2 MSN stimulation elicits distinct BOLD signal changes. Related to Figure 2. **A** Viral targeting of ChR2-EYFP to the vl CPU in A2A-Cre mice and **B** overlay of mean time-series of D1-/D2-/A2A-Cre mice extracted from vl CPU. **C** Unthresholded GLM z-stat activation maps of D2 MSN stimulation. **D** Correlation of D2-Cre and A2A-Cre z-scores of key regions connected to the BG (Pearson's  $r(5)=0.89$ ,  $p=0.007$ ). **E** Correlation of D1-Cre and A2A-Cre z-scores of key regions connected to the BG (Pearson's  $r(5)=0.38$ ,  $p=0.053$ ). D1-Cre time-series depicted in maroon, D2-Cre time-series depicted in teal, A2A-Cre time-series depicted in lilac. Laser stimulation blocks indicated in grey. MOp, primary motor cortex; AI, agranular insula; AAA, anterior amygdalar area; CPU, caudate putamen; SSp-n, primary somatosensory area, nose; TEa, temporal association area; GPi, internal globus pallidus; SCm, superior colliculus, motor related; Crus I; GPe, external globus pallidus; TH, thalamus; STN, subthalamic nucleus; ccb, corpus callosum, body; ctx, cortex. Scale bars, 100 $\mu$ m. N(A2A-Cre)=11, n(D2-Cre)=8.

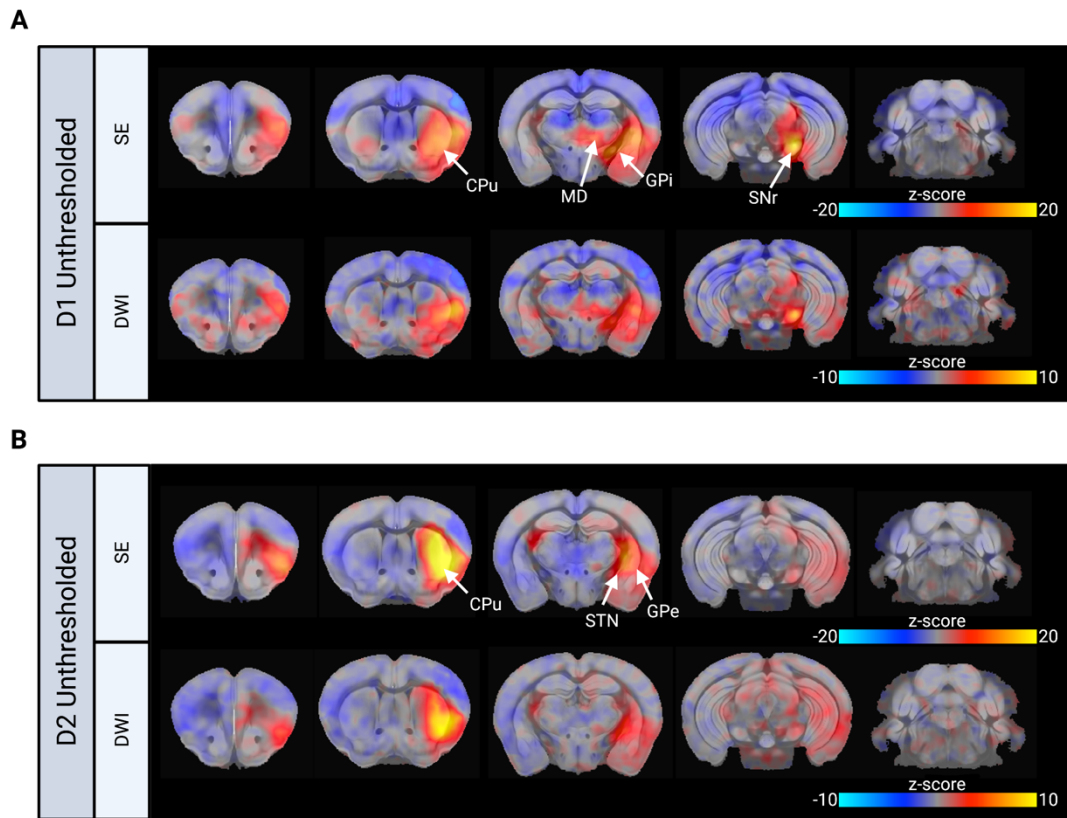


**Figure S5** SE and dfMRI faithfully recapitulate causal influences of D1R and D2R cell activity within the BG. Related to Figure 2. **A** Unthresholded GLM spin-echo (SE) and dfMRI z-stat activation maps of D1R cell stimulation. **B** Unthresholded GLM SE and dfMRI z-stat activation maps of D2R cell stimulation.  $N(\text{D1-Cre})=11$ ,  $n(\text{D2-Cre})=8$ . CPU, caudate putamen; GPe, external globus pallidus; GPi, internal globus pallidus; MD, mediodorsal nucleus of thalamus; STN, subthalamic nucleus; SNr, substantia nigra.



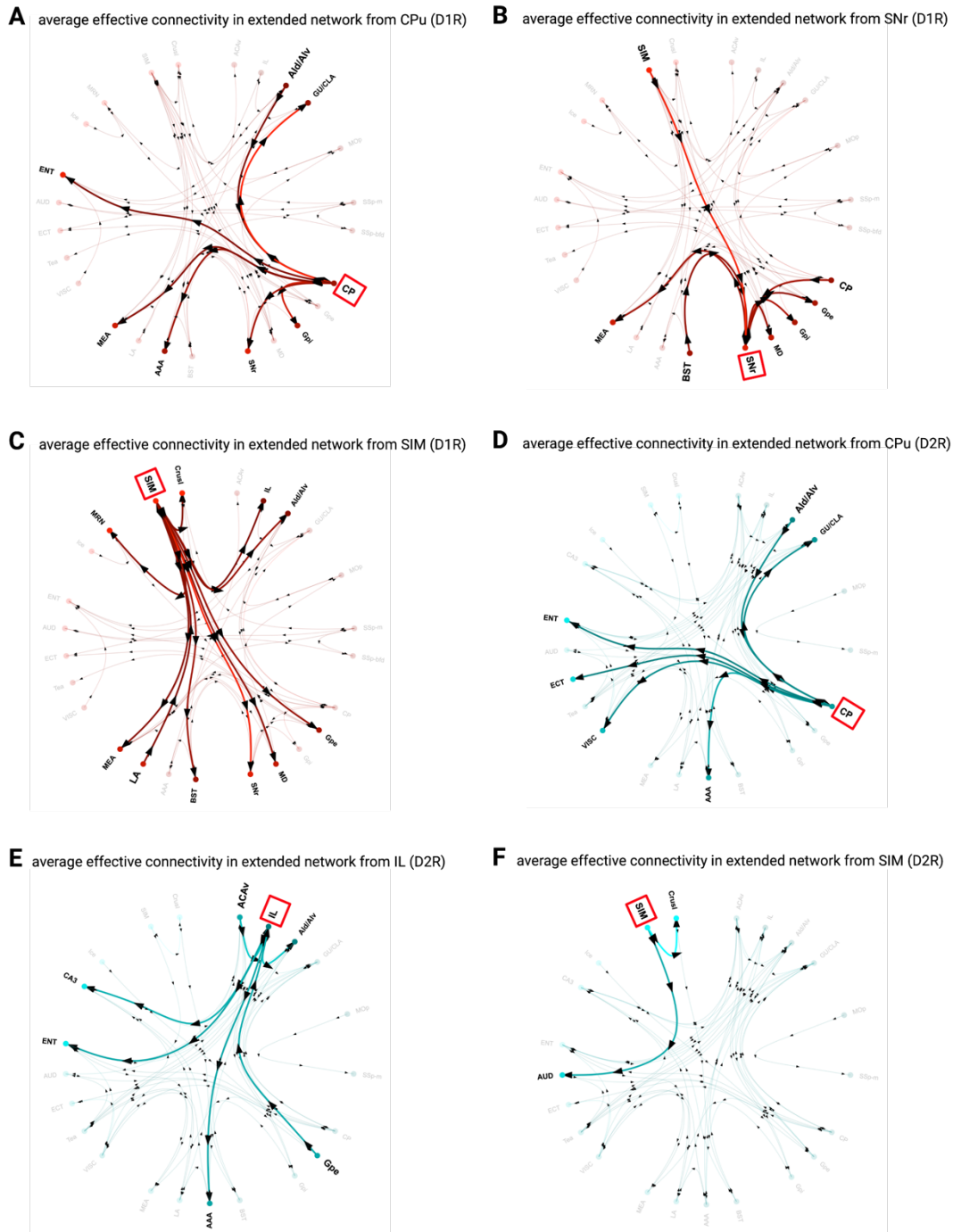


**Figure S6** Maximally and minimally co-activated brain regions upon D1R and D2R cell activation. Related to STAR Methods, rDCM analysis. ACAv, anterior cingulate; IL, infralimbic area; Ald/Alv, agranular insula dorsal/ventral; MOp, primary motor cortex; SSp-m, primary somatosensory cortex, mouth area; SSp-bfd, primary somatosensory cortex, barrel field; GU/CLA, gustatory area/claustrium; CPu, caudate putamen; BST, bed nucleus of tria terminalis; AAA, anterior amygdalar area; GPe, external globus pallidus; GPi, internal globus pallidus; SBPV, subparaventricular zone; SSp-II, primary somatosensory cortex, lower limb; VISC, visceral area; TEa, temporal association area; MD, mediodorsal nucleus of thalamus; LA, lateral amygdalar nucleus; MEA, medial amygdalar nucleus; TU, tuberal nucleus; ECT, ectorhinal area; AUD, auditory area; SNr, substantia nigra; Mmme, medial mammillary nucleus, median part; CA3, cornu ammonis 3; ENT, entorhinal area; ICe, inferior colliculus, external nucleus; MRN, midbrain reticular nucleus; SIM, simple lobule; Crus I.

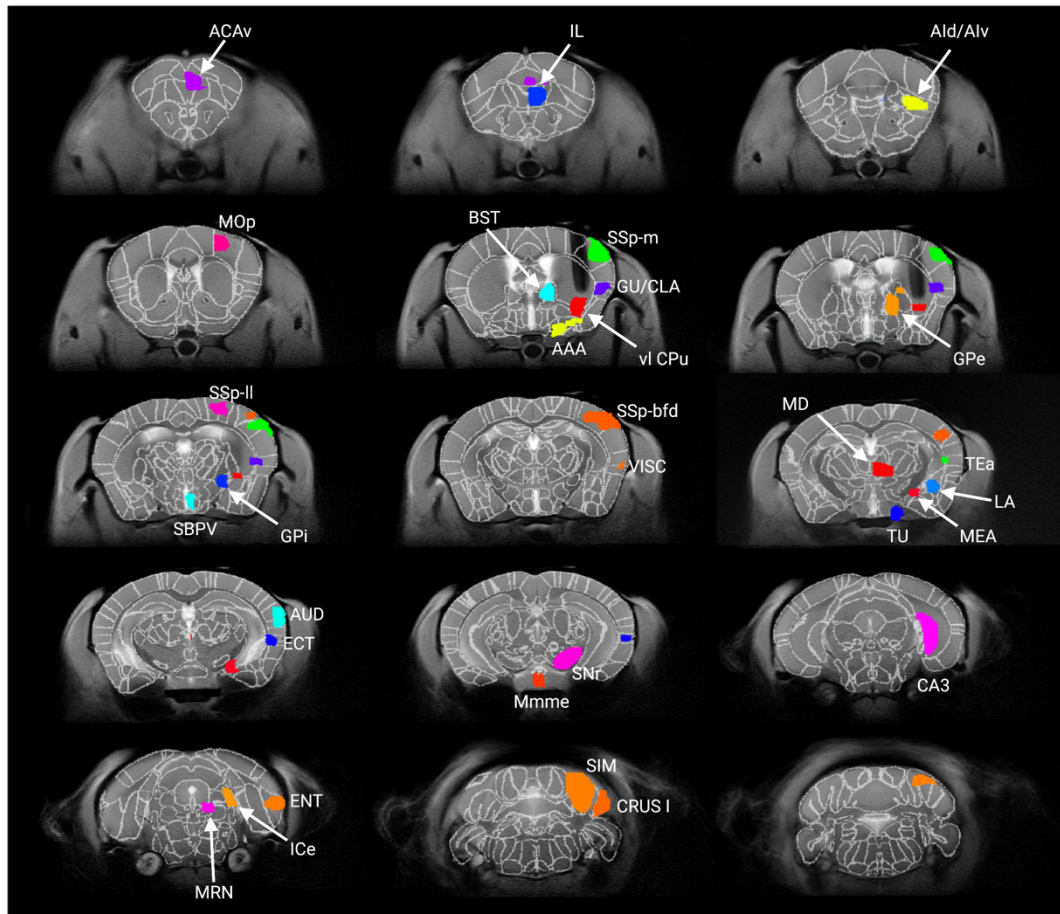


**Figure S7** Whole-brain effective connectivity during D1R and D2R cell stimulation as inferred using regression DCM (rDCM). Related to Figure 5. **A** Average connectivity patterns in the extended network during D1R cell stimulation, from the CPu, **B** from the SNr, and **C** from the SIM ( $P_p > 0.95$ ). **D** Average connectivity patterns in the extended network during D2R cell stimulation, from the IL, and **E** from the SIM ( $P_p > 0.95$ ). Note, circo plots have been adjusted to show 50<sup>th</sup> percentile of increased directed connections only.  $N(\text{D1-Cre})=11$ ,  $n(\text{D2-Cre})=8$ . AAA, anterior amygdalar area; ACAv, anterior cingulate; PrL, prelimbic area; Alv, ventral agranular insula; AUD, auditory area; BST, Bed nuclei of the stria terminalis; CA3, Ammon's horn field 3; CPu, caudate putamen; ECT, ectorhinal area; ENT, entorhinal area; GPe, external globus pallidus; GPi, internal globus pallidus; GU/CLA, gustatory area/claustrium; Ice, inferior colliculus; IL, infralimbic area; LA, lateral amygdala nucleus; MEA, medial amygdala nucleus; MD, mediodorsal nucleus of thalamus; Mmme, medial part of the medial mammillary nucleus; MOp, primary motor cortex; MRN, midbrain reticular nucleus; SIM, simple lobule; SNr, substantia nigra pars reticulata; SBPV, subparaventricular zone; SSp-bfd, primary somatosensory cortex, barrel field; SSp-II, primary somatosensory cortex, lower limb area; SSp-m, primary somatosensory cortex, mouth area; TEa, temporal association area; TU, tuberal nucleus; VISC, visceral area; Crus I.